NASA Contractor Report 189234

Digital Analysis of Wind Tunnel Imagery to Measure Fluid Thickness

Roger L. Easton, Jr. and James Enge
Center for Imaging Science
Rochester Institute of Technology
Rochester, New York 14623-0889

August 1992

Prepared for
Lewis Research Center
Under Grant NAG3-1202

CONTENTS

INTRODUCTION

The lift generated by an airfoil can be disrupted by the presence of viscous fluid on the wing surface. Obviously, the effects are most critical where error margins are smallest, especially during takeoff roll and the early stages of climb to altitude. To study the effects of deicing fluid on lift, the Icing and Cryogenic Technology Branch of the NASA Lewis Research Center conducted more than 300 simulated takeoffs for three different wing models in the Icing Research Tunnel. The model set included two- and three-dimensional models of the Boeing 737 and a two-dimensional model of the deHavilland DASH-8. To avoid any influence of the measurement process on the fluid thickness to be measured, it is necessary to use indirect methods which converting fluid thickness to some remotely measurable physical parameter. The most convenient remote measurements are made by optical means, *e.g.* by adding a fluorescent dye to the deicing fluid and imaging the wing models under ultraviolet illumination. Under such conditions, the fluorescent emission should be directly related to the fluid thickness, *i.e.* the radiation from a thicker fluid should be more intense than from a thinner fluid. In turn, the radiation from a thicker fluid would generate a photographic negative with greater optical density. For a monotonic relationship between thickness and density, it is possible to convert a measurement of film density to emitted radiance from the fluid, and thus to fluid thickness. The conversion from density to fluid thickness may not be trivial because of the nonlinearities of the entire recording process, especially as indicated by the characteristic curve of the photographic emulsion which relates exposure (light intensity multiplied by exposure time) to recorded density. To provide the necessary calibration for the conversion, each simulated takeoff run included a calibration frame of a metal plate with grooves of known depth from 0.25 mm to 4 mm. The plate was photographed in similar fashion to the simulated takeoffs. The densities measured from the calibration plate were to be used as markers to convert measured densities of the wing images to thicknesses. The calibration was applied to three images taken at selected times in the simulated takeoff run.

Historically, the image density measurements have been made with an optical microdensitometer. The variable aperture size and integration time of such a system allows precise measurements of density to be made on a microscopic scale. The precision is gained at the cost of speed; it may be feasible to scan a single line of an image relatively quickly, but microdensitometer scans of a complete image may require many minutes, or even a few hours. Because of the volume of data to be analyzed, as well as other problems with the imagery, measurements by conventional microdensitometer were deemed impractical for this application. Fortunately, new imaging detectors based on charge-coupled devices (CCDs) are available which allow the measurements formerly made in series by a microdensitometer to be made in parallel with adequate spatial resolution and signal-to-noise ratio to allow appropriate analysis. The CCD detector can be combined with a capable personal computer for image analysis. This report describes a procedure that was developed to analyze the images to calculate the fluid thickness by digital imaging techniques.

The measurement procedure was applied to approximately 1300 images supplied by the Icing and Cryogenic Technology Branch to map thicknesses of deicing fluids during simulated takeoffs for the three wing models. The tests were run under various icing conditions in the NASA Lewis Icing Research Tunnel. The images were digitized to a resolution of 1280 samples and 1024 rows (approximately $1.3 \cdot 10^6$ pixels per image) with a *Hawkeye-II*(TM) CCD digital electronic camera supplied by the Eastman Kodak Company. The digital data was analyzed on an IBM-compatible personal computer using an Intel 80386 processor with 80387 mathematical coprocessor. The digitized calibration image (grooved plate) was used to determine the relationship between emulsion transmittance and fluid thickness. The calibration function was used to compute fluid thickness along selected wing chords in each frame to be analyzed in the takeoff run. The plot of fluid thickness was further analyzed to compute the mean and variance of fluid thickness in the specific area of interest between 0.50 and 0.55 of the wing chord.

MEASUREMENT PROCEDURE

The images were digitized with the Kodak *Hawkeye-II*(TM) digital electronic camera, which uses a Kodak MegaPixel (TM) CCD chip as the photosensitive element. The chip has 1280 x 1024 monochrome elements. The camera is composed of a standard Nikon F3 body, a custom-fabricated camera back which contains the CCD chip, and a separate unit which includes the control panel for the camera and a 100-megabyte hard disk drive for image storage. The camera accepts standard Nikkor (TM) lenses; the 55 mm Micro-Nikkor (TM) was used for the measurements in this study. Because the sensitive area of the CCD chip is smaller than a standard 35 mm frame (approximately 10 mm x 13 mm *vs.* 24 mm x 36 mm), a special focusing screen with a customized reticle is installed which allows the user to appropriately frame the scene to be recorded.

The image is exposed in nearly identical fashion to a normal 35 mm film camera, except that the incident photons create free electrons in the CCD elements. The electrons are counted by electron current amplifiers to give a measure of the incident radiation. The electron current is quantized to 8 bits (1 byte) of dynamic range, which gives 256 monochrome brightness levels. The dynamic range of 1 byte per pixel translates to a total of 1280 x 1024 bytes per image, or approximately 1.3 megabytes. The hard drive in the control unit has a capacity of 100 megabytes, so that approximately 75 images may be recorded and stored before transferring the data to the pc for analysis. The transfer of the digitized image to the camera hard drive requires less than five seconds, and thus image data may be gathered quite rapidly. The camera system is mounted on a standard Polaroid MP-4 copy stand. The camera height was chosen so that the scale of the digitized image is approximately 25 pixels per mm on the film, which means in turn that approximately 40 mm by 50 mm of the original film could be digitized.

The images from the wind-tunnel tests had been recorded on long rolls of 70 mm Kodak TRI-X film. The rolls were protected by transparent sleeving. For digitization, each film was removed from its sleeve and rolled onto 70 mm spools. A 70 mm film transport was mounted on a small light box and used to carry the film spools, thus allowing accurately repeatable positioning of the film images. The illumination of the light box was determined to be very uniform (measurable variation only near the edges of less than 10%). Tests also were conducted to determine the linear dynamic range of the digitizing camera. The system was demonstrated to be very linear in intensity transmittance τ over the range $1 \leq \tau \leq 0.01$, which translates to a density range $0 \leq D \leq 2$.

The camera system is interfaced to an IBM-compatible personal computer through a Small Computer Standard Interface (SCSI) port, which allows images to be transferred to the PC for storage and analysis. The PC is equipped with a 140-megabyte hard drive, with 100 megabytes set aside for image storage. Thus a full disk of images on the camera could be "dumped" at one time to the PC for analysis. The data transfer rate from the camera disk to the computer disk is limited by the SCSI data rate so that approximately 15 seconds are required to transfer one image from the camera disk to the PC disk. A magnetic tape backup from Colorado Memory Systems was purchased for archival image storage. A single tape can store 120 megabytes of uncompressed data or up to 250 megabytes of compressed data per tape. The data transfer rate to tape is extremely slow; about 25 seconds are required to transfer one image, or 30 minutes for a full disk of 80 images. If selected, the optional software data compression added little time to the transfer to tape. However, because the compression algorithm is optimized for text, only about 20% - 30% of storage capacity was saved, and the price paid was quite high as the retrieval time for compressed data was larger than for uncompressed data by more than a factor of two.

The images from the CCD camera were displayed on a standard VGA color monitor, which has a spatial resolution of 640 by 480 picture elements and a brightness resolution of 16 monochrome gray levels. It is thus not possible to display the entire CCD image on the monitor at full brightness resolution. Software was written to display the image at reduced spatial and brightness resolution so that the appropriate regions of the image could be selected for analysis. These full-resolution data from the selected areas can be analyzed and the appropriate statistics computed.

After a sequence of four images has been digitized and transferred to the PC, the data was analyzed. The image of the calibration plate was displayed and the mean and variance of gray level was calculated for each of the 17 thicknesses regions (0 mm to 4 mm in increments of 0.25 mm). Segments of a region that had been poorly illuminated were not included in the computation of the statistics. The measurement of the gray level of the zero-thickness region was usually uncertain. It seems likely that "puddles" of fluid remained on the surface of the calibration plate during exposure, which made interpretation of the images more difficult. The statistics were entered into a program to generate the lookup table for the thickness calibration. The digitized images from the takeoff run were displayed in sequence on the PC at reduced resolution and a chord selected for analysis. The data from the chord line was written to a file and stored. The calibration lookup table and the data file were then applied as inputs to software which had been written to perform the thickness computation of the data and compute the desired statistics. The thickness data were displayed and printed, and the mean and variance of the thickness was computed. A compilation of the thickness measurements is presented in Appendix A.

A subset of image sequences was selected for further processing. These images were converted to a format with full brightness and reduced spatial resolution for display on an Imaging Technology Overlay Frame Grabber(TM) using the ImageLab(TM) image processing software package from Werner Frei Associates. The images were displayed and printed using a pseudocolor mapping of fluid thickness. The processing of one image sequence is shown in detail.

To quantify the limitations of the processes of digitization and image analysis, a series of preliminary tests were performed to measure the uniformity of the illumination from the light box, and to measure the linear dynamic range of the HAWKEYE-II (TM) camera. A nominally uniform field from the light box was digitized and the gray levels measured to estimate the illumination uniformity. The field was measured to be uniform to within 10% at the extreme corners of the field. Over the area of interest, the field was uniform to within 3%. The HAWKEYE-II (TM) camera was measured to be uniform over a transmission range of 0.01 to 1, or a range of film density of approximately two. Though less than the linear range obtainable from a microdensitometer, this dynamic range was deemed sufficient for the film data available.

SOFTWARE

To compute the calibration lookup table and analyze the data from the selected wing chords, a program was written for the PC in MicroSoft QuickBASIC (TM) Version 4.5. The program computes the interpolated lookup table from the gray-level statistics of the calibration plate from a data file containing the mean gray values of the 17 thickness segments of the calibration plate. The data are interpolated with a user-selected function to compute the lookup table of fluid thickness corresponding to each of 256 gray levels. The selectable interpolation functions include zero-order interpolation with a rectangle function (also known as nearest-neighbor interpolation), first-order interpolation with a triangle function, second-order interpolation with a cubic function, and ideal interpolation with the sinc function. A test with simulated data demonstrated that linear interpolation gave the smoothest lookup table, which is the most likely result from physical considerations. The lookup table may be stored as a 256-element data file for later analysis. The wing chord data file is transformed through the lookup table, the statistics are computed, and the results displayed. The statistics are written to the file of statistical data.

The software is included with the digital data files and is available as source code on disk by written request to the author.

RESULTS

The data and analysis for run 227 of the de Havilland Dash-8 wing model are shown in detail in this section, and the measurements of the entire data set are presented in tabular form in the Appendix. This was a typical "good" data set in that the calibration data set was monotonic. The image of the calibration plate was digitized and the gray-level mean and variance computed for the 16 sections of thickness 0.25 mm to 4 mm and for the uncovered surface (fluid thickness of 0 mm). The lookup table from gray level to thickness was computed from the measurements of the calibration plate. The first step was to interpolate the gray levels of the 17 thicknesses to a total of 256 increments over the full thickness range. The resulting lookup table estimates the gray level corresponding to each of 256 thicknesses τ in the interval $0 \text{ mm} \leq \tau \leq 4 \text{ mm}$. This table was "inverted" by exchanging the rows and columns to generate the estimated thickness from the measured gray level.

In some cases, the data from the interpolated lookup table before inversion was not monotonic, *i.e.* the gray level decreased with thickness to a minimum, and then increased with thickness. This is most likely due to solarization of the emulsion due to intense overexposure. To understand this effect, consider the characteristic curve of a photographic emulsion, as illustrated in Figure 1. The curve is a plot of the density D of the photographic negative which would be obtained for different log exposures, where exposure E is defined as irradiance I multiplied by time T. The curve may be divided into five arbitrary regions:

1. the underexposed region, where an increase in log E does not change the recorded density D.
2. The "toe" of the curve, where an increase in log E produces a gradual increase in slope of the log E - D curve.
3. The linear part of the curve, where log E and D are proportional.
4. The "shoulder" of the curve, where an increase in log E produces a gradual decrease in slope.
5. The reversal or solarization region, where an increase in log E generates a reduced density D, so that the slope of D *vs.* log E is negative.

Because of the apparent difficulty in accurately estimating the emitted radiance of the fluid, the photographic images in this project were exposed on the "shoulder" of the characteristic curve, *i.e.* the images were generally overexposed. In some cases, overexposure was extreme enough to solarize the image. In solarization, the incident radiation interacts to generate free halogen in the emulsion which "shields" the latent image from development. Thus many of the overexposed photographic grains are not converted to silver, which results in a decrease in density with increasing exposure. In the solarized images, an area of near-maximum density may have been generated by exposure on the shoulder or in the solarized region. Thus the lookup table is double-valued and may not be inverted. When this effect occurred in the data, the solarization region was rejected to force the data to be single-valued so that the thickness maps are biased toward lower values.

If a similar experiment is performed in the future with film as the detector, care should be taken to prevent solarization by ensuring that the film is exposed on the linear portion of the characteristic curve.

The input data and computed lookup tables for Run 227 are shown in Figure 2. Note that the "negatives" were digitized so that the low gray levels occur in the denser regions of the negative, which are due to the emitted radiance from thick fluid. Because the exposure is up on the "shoulder" of the characteristic curve, a large change in thickness results in a small change in gray level. In the inverted lookup table, the slope of the calibration curve of gray

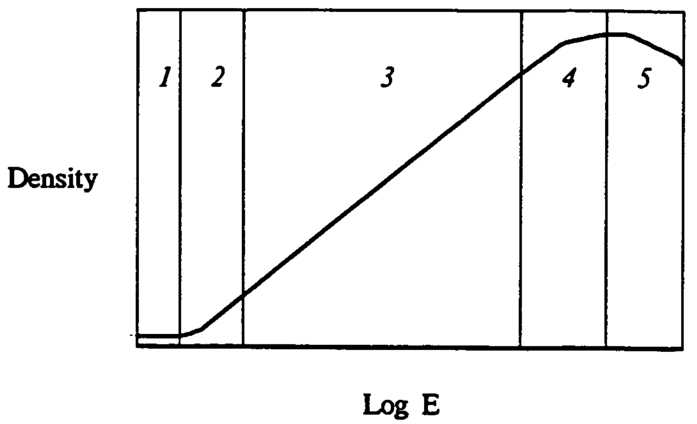

Figure 1: Characteristic Curve of Typical Photographic Film

level *vs.* thickness is quite steep for large thicknesses, and thus the precision of the measurement is most uncertain for large thicknesses. This is demonstrated most clearly in cases where the slope of the lookup table was very steep for thick fluid concentrations. If thick regions exist on the wing images, the chord thickness map is visibly quantized, *i.e.* a change in measured radiance of a single gray level transforms through the lookup table to a large change in thickness. This is due to the overexposure of the film and cannot be compensated by *a posteriori* means.

After computing the calibration lookup table, the other three digitized images of the run were displayed in sequence and the gray levels of a chord were read into a data file. Care was taken to ensure that the same (or nearly the same) chord was used each time, within the constraints of the quality of the individual images. If the image exhibited regions of nonuniform exposure in the area of the selected chord, a different but nearby chord was used. Fortunately, this was usually not a problem. The statistics of the chord were calculated by the program. The raw data and the transformed thickness maps of the chord from Run 227, Frame 722 are shown in Figure 3. Note that darker areas of the raw data indicate regions of thicker fluid concentration.

The thickness calibration can also be applied to the entire wing image so that the monochrome gray level of the image is proportional to the fluid thickness. Such an image theoretically conveys all the information available. However, the brightness resolution of the human eye in monochrome is quite limited; it has been estimated that an adapted eye can distinguish approximately 50-70 levels. This thus restricts the information actually visible. However, the eye can distinguish many colors, and it is quite common to remap an image with subtle changes in gray level to pseudocolor to make the information more visible. Selected images of the Dash-8 were displayed in pseudocolor using the Werner Frei *ImageLAB* image processing software package from Werner Frei Associates of Venice, California. This is a PC-based system which uses the Overlay Frame Grabber from Imaging Technology. Only a 512 row by 512 column image may be displayed, so the images were decimated before mapping. The monochrome and pseudocolor calibrated image sequences for Run 227, including the calibration plate and three chord images, are shown in Figure 4 and Figure 5, respectively. In the pseudocolor mapping, the colors were selected to match the first four thickness levels, *i.e.* red denotes thicknesses of 0.25 mm, green to 0.5 mm, light blue to 0.75 mm, and dark blue to regions of thickness greater than or equal to 1 mm. The steep slope of the lookup table for large thickness made it difficult to assign colors unambiguously.

Due to the volume of data, the complete set of thickness maps for all runs is not included in this report. The maps have been transmitted to the Icing and Cryogenic Technology Branch of the NASA Lewis Research Center and are also available upon request.

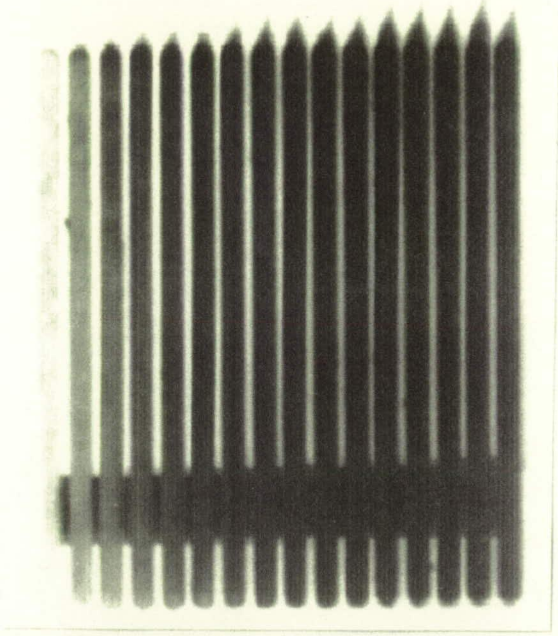

a. Digitized Raw Image

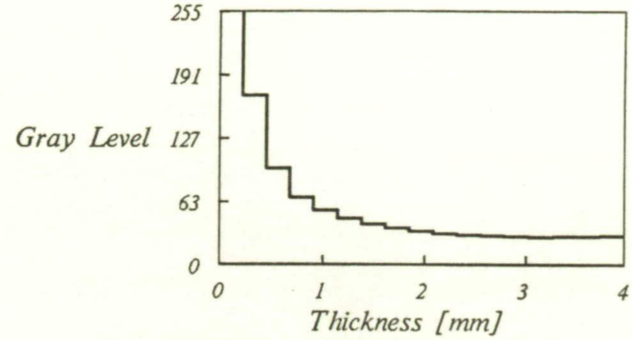

b. Gray Level vs. Thickness

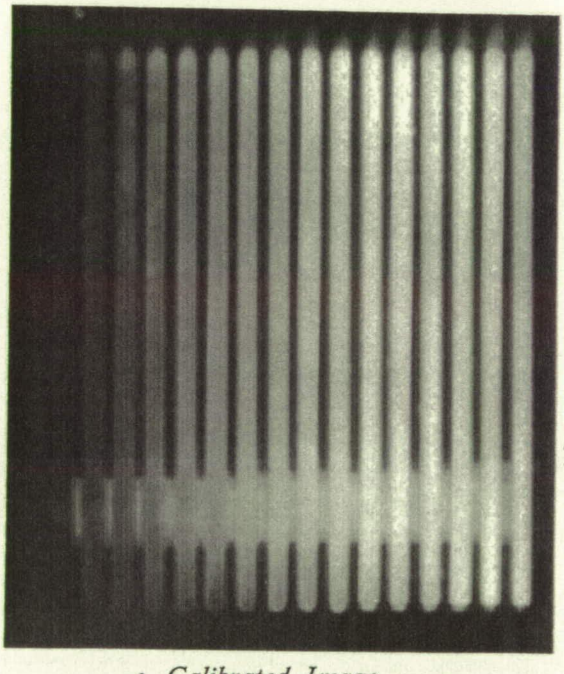

c. Calibrated Image
(gray level proportional to thickness)

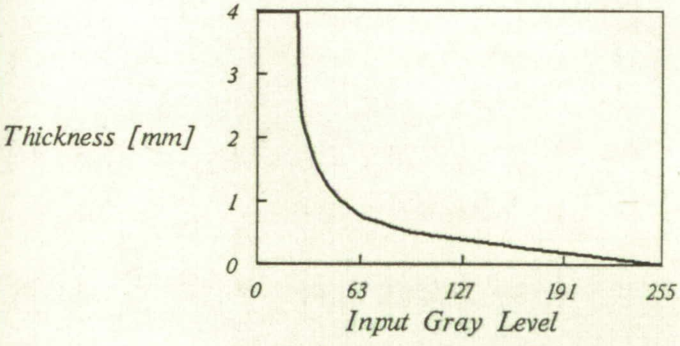

d. Calibration Lookup Table

Figure 2: Calibration of Run 227

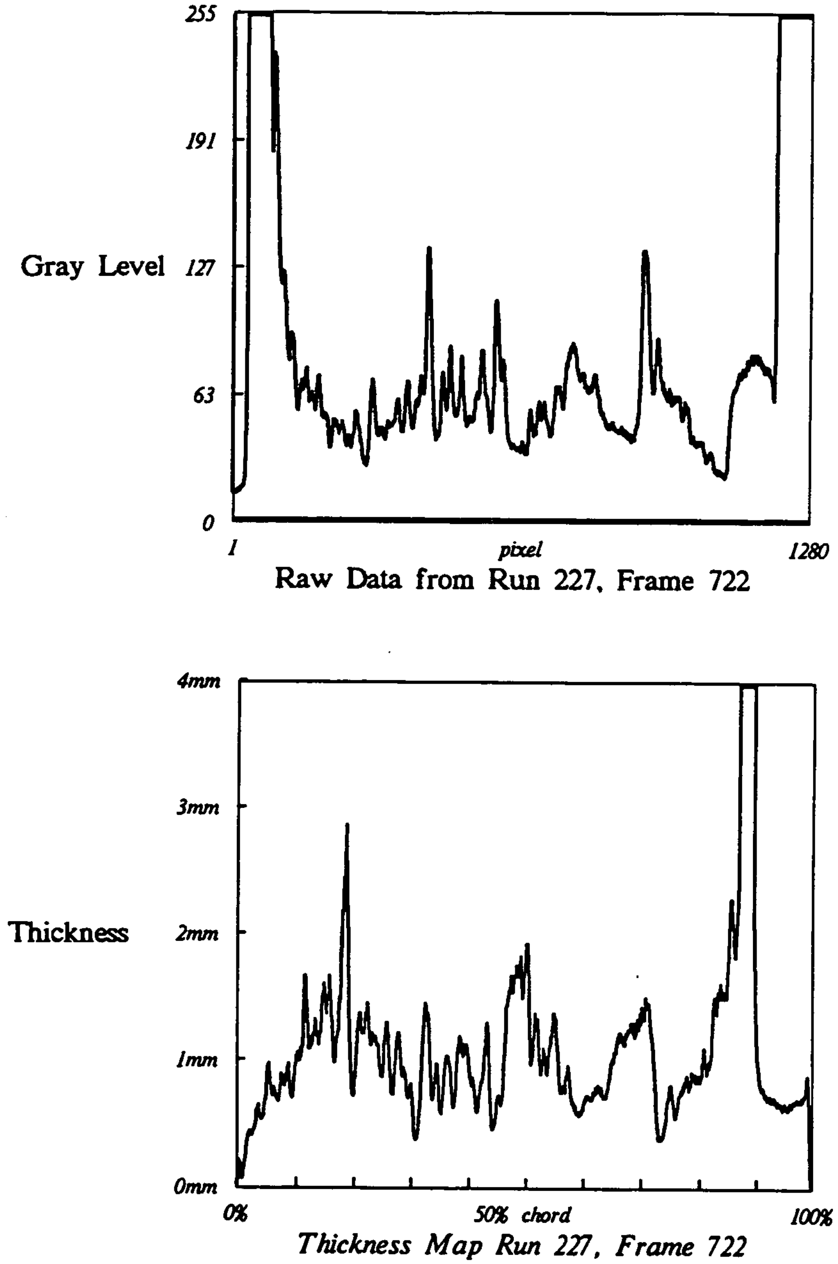

Raw Data from Run 227, Frame 722

Thickness Map Run 227, Frame 722

Figure 3 -- Run 227, Frame 722, Raw Data (top) and Thickness Map (bottom)

ORIGINAL PAGE
BLACK AND WHITE PHOTOGRAPH

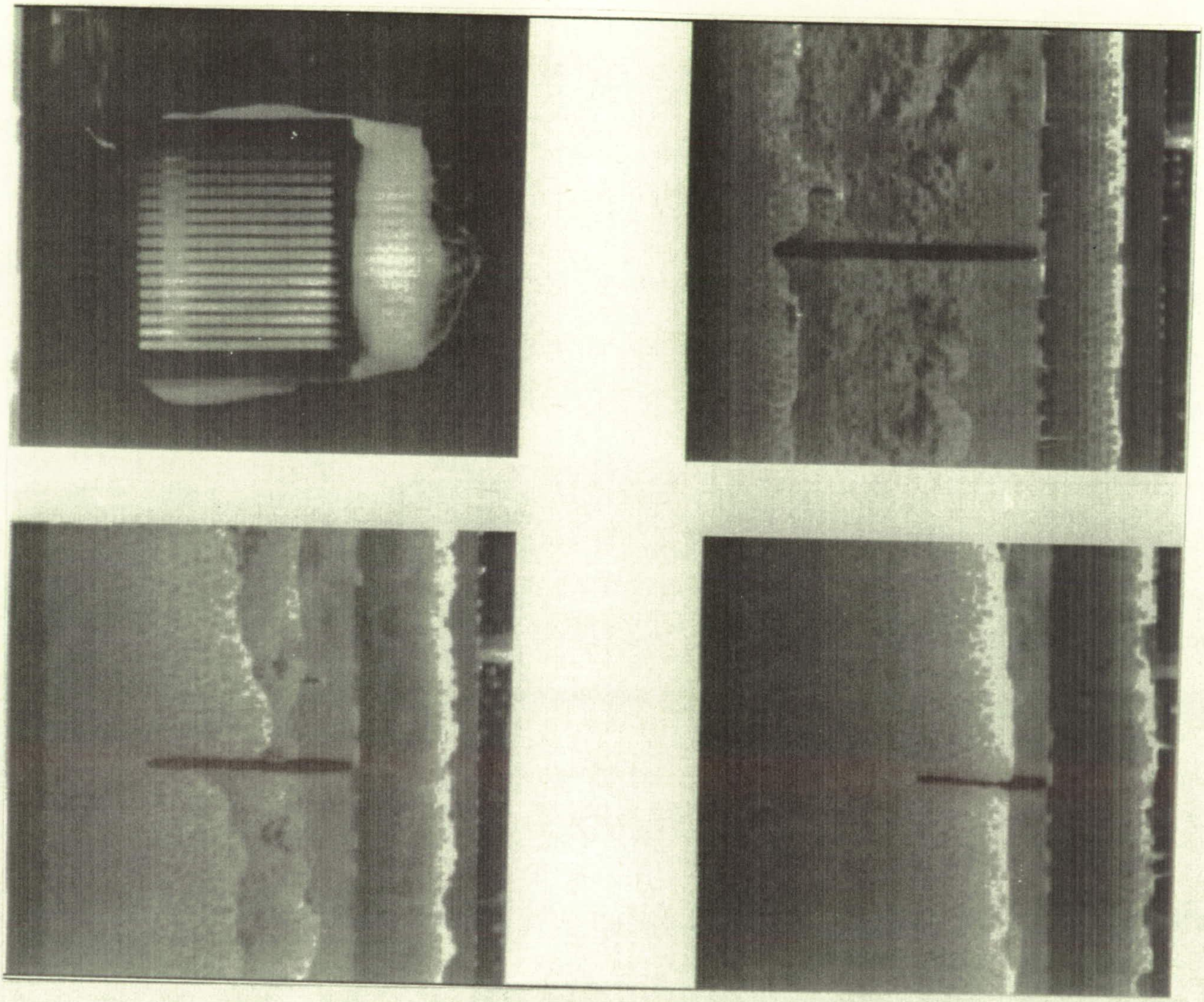

Figure 4: Monochrome Image Sequence for Run 227 After Calibration
Upper Left -- Calibration Plate
Upper Right -- Wing Image Taken 10 Seconds After Roll
Lower Left -- Wing Image Taken 13 Seconds After Roll
Lower Right -- Wing Image Taken 16 Seconds After Roll

ORIGINAL PAGE
COLOR PHOTOGRAPH

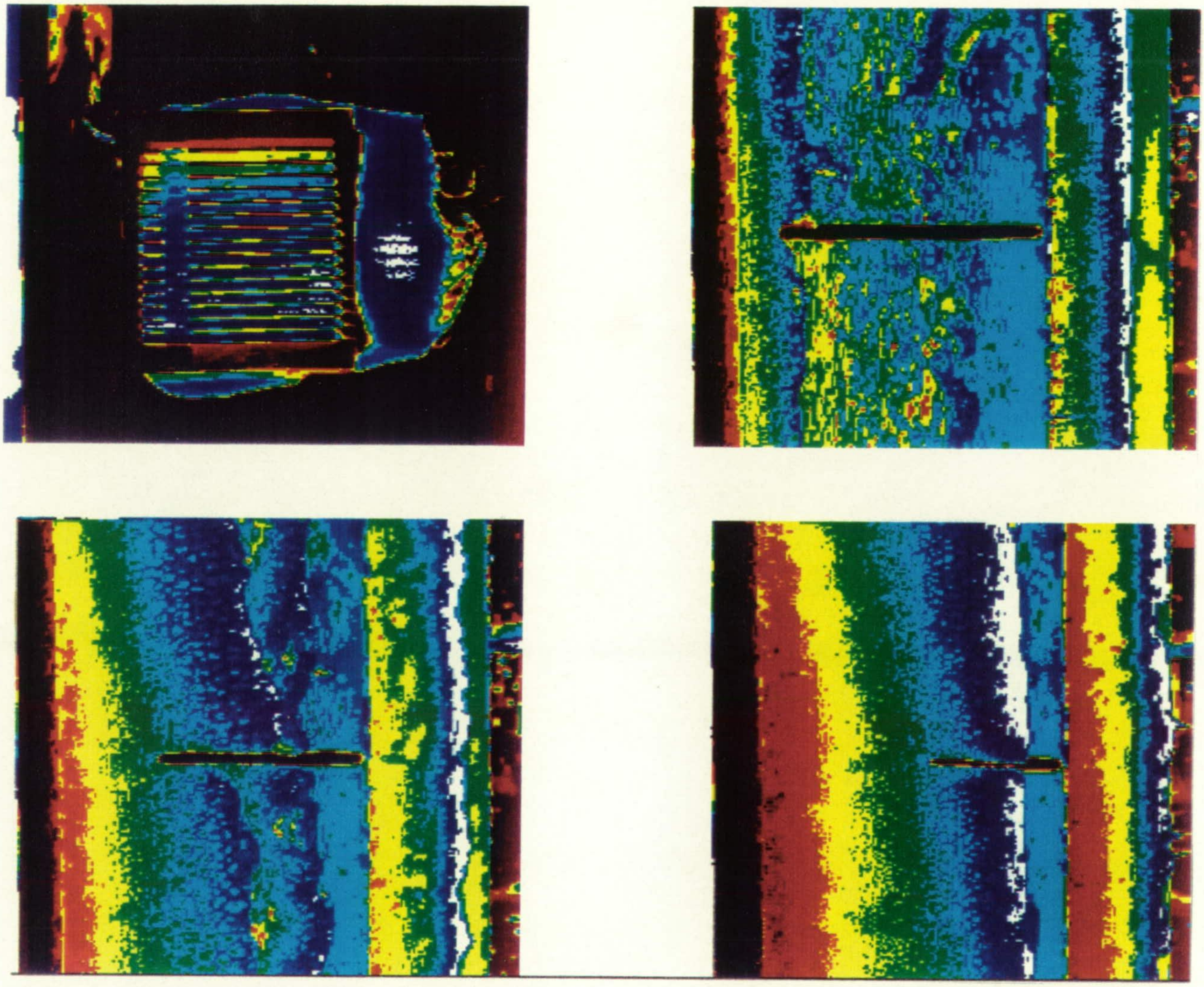

Figure 5: Pseudocolor Image Sequence for Run 227
Upper Left -- Calibration Plate
Upper Right -- Wing Image Taken 10 Seconds After Roll
Lower Left -- Wing Image Taken 13 Seconds After Roll
Lower Right -- Wing Image Taken 16 Seconds After Roll

RECOMMENDATIONS

The experimental procedure for gathering the original data set and analyzing the images is fundamentally sound, but the results indicate that the effort was not entirely successful. This was due primarily to the limitations of the photographic film used for the original images, and most fundamentally to its nonlinear response. The requirements of brightly illuminating the experimental scene at short intervals made it difficult to precisely estimate the exposure setting for the film each time. As a result, the film was often overexposed, and occasionally to the point where solarization occurred. In either of these cases, the precision of measurement in the thickest regions of the fluid is limited. In addition, the images of the calibration plate must be obtained under absolutely repeatable conditions, i.e. the surface of the plate must be entirely free from fluid so that an accurate determination of the gray level for zero thickness can be made.

As a result of this effort, we propose the following recommendations for any future measurements.

1. To avoid the difficulties resulting from the nonlinear response of photographic film, we recommend that an electronic imaging system using a charge-coupled device (CCD) detector be used to gather data. Such systems are now available with sufficient spatial resolution (up to 2000 picture elements) from several vendors, including Eastman Kodak. CCD cameras may be used in linear mode so that the gray level of a pixel will be proportional to the incident irradiance. The images can be stored rapidly and examined immediately. Though the cameras are still expensive ($10,000 or more), the cost of film and subsequent digitization is eliminated.

2. One constraint on this effort was the limited resolution and data capacity of the computer. Since this effort was carried out, new inexpensive systems which can display full-resolution images are available which can read the images from the new CCD cameras directly.

3. A measurement of the actual illumination for each exposure would allow variations to be compensated. A simple photocell could be positioned in the scene and its output recorded. Multiple detectors at different points in the scene could be used to measure coarse nonuniformities in illumination.

4. If feasible, a calibration should be included in every frame to ensure the precision of the thickness mapping. It could be attached to the wing model if this did not interfere with the air flow.

APPENDIX: STATISTICS OF THICKNESS MEASUREMENTS

The normalized statistics (mean and variance) of the thickness in the range of 0.5 - 0.55 of chord are tabulated for all runs of the three wing models.

Statistics File for Wing Data, Boeing 737, 3-D model

μ = mean thickness in chord interval 50%-55% [mm]
Normalized Mean = Mean/305mm
σ = standard deviation of mean value [mm]

Run-Frame	μ [mm]	μ/length	σ [mm]	t [seconds]
R70-048	0.173	$5.69 \cdot 10^{-4}$	0.112	10
R70-052	0.086	$2.82 \cdot 10^{-4}$	0.020	23
R70-054	0.168	$5.52 \cdot 10^{-4}$	0.017	26
R71-077	0.488	$1.60 \cdot 10^{-3}$	0.027	10
R71-081	0.137	$4.50 \cdot 10^{-4}$	0.071	23
R71-083	0.179	$5.88 \cdot 10^{-4}$	0.154	26
R72-108B	0.423	$1.39 \cdot 10^{-3}$	0.338	10
R72-113B	0.168	$5.49 \cdot 10^{-4}$	0.018	23
R72-114B	0.208	$6.82 \cdot 10^{-4}$	0.057	26
R80-170	0.109	$3.56 \cdot 10^{-4}$	0.011	10
R80-176	0.072	$2.36 \cdot 10^{-4}$	0.014	29
R80-177	0.072	$2.36 \cdot 10^{-4}$	0.015	32
R81-200	0.352	$1.15 \cdot 10^{-3}$	0.158	10
R81-204	0.162	$5.30 \cdot 10^{-4}$	0.015	23
R81-205	0.150	$4.91 \cdot 10^{-4}$	0.012	26
R83-223	0.653	$2.14 \cdot 10^{-3}$	0.118	10
R83-227	0.164	$5.36 \cdot 10^{-4}$	0.039	23
R83-228	0.126	$4.13 \cdot 10^{-4}$	0.029	26
R84-253	0.600	$1.97 \cdot 10^{-3}$	0.487	10
R84-257	0.174	$5.70 \cdot 10^{-4}$	0.022	23
R84-258	0.186	$6.09 \cdot 10^{-4}$	0.018	26
R86-276	0.417	$1.37 \cdot 10^{-3}$	0.286	10
R86-280	0.123	$4.02 \cdot 10^{-4}$	0.020	23
R86-281	0.094	$3.09 \cdot 10^{-4}$	0.023	26
R87-299	0.277	$9.07 \cdot 10^{-4}$	0.085	10
R87-303	0.156	$5.12 \cdot 10^{-4}$	0.020	23
R87-304	0.175	$5.72 \cdot 10^{-4}$	0.024	26
R93-319	0.660	$2.16 \cdot 10^{-3}$	0.073	10
R93-323	0.192	$6.30 \cdot 10^{-4}$	0.034	23
R93-324	0.148	$4.86 \cdot 10^{-4}$	0.012	26

Run-Frame	μ [mm]	μ/length	σ [mm]	t [seconds]
R94-344	0.156	$5.12\cdot10^{-4}$	0.023	10
R94-348	0.067	$2.20\cdot10^{-4}$	0.039	23
R94-349	0.126	$4.14\cdot10^{-4}$	0.051	26
R95-370	0.199	$6.54\cdot10^{-4}$	0.044	10
R95-374	0.132	$4.34\cdot10^{-4}$	0.042	23
R95-375	0.095	$3.13\cdot10^{-4}$	0.022	26
R97-386	0.107	$3.50\cdot10^{-4}$	0.026	10
R97-390	0.048	$1.59\cdot10^{-4}$	0.013	23
R97-391	0.051	$1.67\cdot10^{-4}$	0.021	26
R98-418	0.298	$9.78\cdot10^{-4}$	0.176	10
R98-421	0.197	$6.47\cdot10^{-4}$	0.017	20
R98-422	0.233	$7.63\cdot10^{-4}$	0.031	23
R100-435	0.279	$9.14\cdot10^{-4}$	0.194	10
R100-439	0.089	$2.93\cdot10^{-4}$	0.016	23
R100-440	0.090	$2.96\cdot10^{-4}$	0.021	26
R101-456	0.283	$9.27\cdot10^{-4}$	0.062	10
R101-460	0.115	$3.78\cdot10^{-4}$	0.023	23
R101-461	0.106	$3.48\cdot10^{-4}$	0.018	26
R102-479	0.149	$4.89\cdot10^{-4}$	0.023	10
R102-483	0.117	$3.85\cdot10^{-4}$	0.016	23
R102-484	0.124	$4.07\cdot10^{-4}$	0.020	26
R110-506	0.213	$6.98\cdot10^{-4}$	0.082	10
R110-514	0.210	$6.90\cdot10^{-4}$	0.026	23
R110-516	0.310	$1.02\cdot10^{-3}$	0.069	26
R112-551	0.256	$8.39\cdot10^{-4}$	0.302	10
R112-555	0.134	$4.40\cdot10^{-4}$	0.010	23
R112-556	0.173	$5.68\cdot10^{-4}$	0.014	26
R114-546	0.536	$1.76\cdot10^{-3}$	0.106	10
R114-550	0.217	$7.12\cdot10^{-4}$	0.136	23
R114-551	0.131	$4.30\cdot10^{-4}$	0.022	26
R115-567	0.203	$6.67\cdot10^{-4}$	0.008	10
R115-571	0.093	$3.04\cdot10^{-4}$	0.022	23
R115-572	0.097	$3.18\cdot10^{-4}$	0.022	26
R116-588	0.495	$1.62\cdot10^{-3}$	0.437	10
R116-592	0.115	$3.78\cdot10^{-4}$	0.040	23
R116-593	0.116	$3.80\cdot10^{-4}$	0.038	26

Run-Frame	μ [mm]	μ/length	σ [mm]	t [seconds]
R120-611	0.446	$1.46 \cdot 10^{-3}$	0.050	10
R120-615	0.124	$4.07 \cdot 10^{-4}$	0.028	23
R120-616	0.112	$3.68 \cdot 10^{-4}$	0.031	26
R121-636	0.522	$1.71 \cdot 10^{-3}$	0.096	10
R121-640	0.195	$6.39 \cdot 10^{-4}$	0.042	23
R121-641	0.199	$6.53 \cdot 10^{-4}$	0.044	26
R123-657	0.525	$1.72 \cdot 10^{-3}$	0.104	10
R123-661	0.113	$3.69 \cdot 10^{-4}$	0.020	23
R123-662	0.095	$3.11 \cdot 10^{-4}$	0.018	26
R124-675	1.378	$4.52 \cdot 10^{-3}$	1.182	10
R124-679	0.206	$6.76 \cdot 10^{-4}$	0.022	23
R124-680	0.145	$4.74 \cdot 10^{-4}$	0.015	26
R126-701	0.198	$6.48 \cdot 10^{-4}$	0.018	10
R126-702	0.244	$8.00 \cdot 10^{-4}$	0.053	23
R126-703	0.347	$1.14 \cdot 10^{-3}$	0.102	26
R127-718	0.166	$5.43 \cdot 10^{-4}$	0.016	10
R127-722	0.083	$2.71 \cdot 10^{-4}$	0.025	23
R127-723	0.074	$2.43 \cdot 10^{-4}$	0.012	26
R128-741	0.198	$6.49 \cdot 10^{-4}$	0.030	10
R128-745	0.128	$4.21 \cdot 10^{-4}$	0.018	23
R128-746	0.122	$4.01 \cdot 10^{-4}$	0.023	26
R137-765	1.127	$3.69 \cdot 10^{-3}$	0.114	10
R137-772	0.912	$2.99 \cdot 10^{-3}$	0.057	29
R137-773	0.926	$3.04 \cdot 10^{-3}$	0.032	32
R138-788	0.455	$1.49 \cdot 10^{-3}$	0.125	10
R138-792	0.220	$7.20 \cdot 10^{-4}$	0.120	23
R138-793	0.162	$5.33 \cdot 10^{-4}$	0.010	26
R140-809	0.513	$1.68 \cdot 10^{-3}$	0.317	10
R140-813	0.326	$1.07 \cdot 10^{-3}$	0.262	23
R140-814	0.187	$6.12 \cdot 10^{-4}$	0.022	26
R141-832	0.257	$8.44 \cdot 10^{-4}$	0.178	10
R141-836	0.103	$3.38 \cdot 10^{-4}$	0.013	22
R141-837	0.123	$4.04 \cdot 10^{-4}$	0.016	25
R142-854	0.327	$1.07 \cdot 10^{-3}$	0.114	10
R142-858	0.128	$4.21 \cdot 10^{-4}$	0.010	23
R142-859	0.107	$3.49 \cdot 10^{-4}$	0.013	26

Run-Frame	μ [mm]	μ/length	σ [mm]	t [seconds]
R144-878	0.679	$2.23 \cdot 10^{-3}$	0.385	10
R144-882	0.157	$5.13 \cdot 10^{-4}$	0.062	23
R144-883	0.095	$3.11 \cdot 10^{-4}$	0.016	26
R145-900	0.492	$1.61 \cdot 10^{-3}$	0.109	10
R145-904	0.097	$3.19 \cdot 10^{-4}$	0.013	23
R145-905	0.086	$2.81 \cdot 10^{-4}$	0.017	26
R146-924	0.201	$6.61 \cdot 10^{-4}$	0.100	10
R146-928	0.117	$3.83 \cdot 10^{-4}$	0.020	23
R146-929	0.098	$3.22 \cdot 10^{-4}$	0.019	26
R148-941	0.225	$7.37 \cdot 10^{-4}$	0.014	10
R148-943	0.296	$9.70 \cdot 10^{-4}$	0.121	16
R148-944	0.228	$7.48 \cdot 10^{-4}$	0.084	19
R149-960	0.656	$2.15 \cdot 10^{-3}$	0.225	10
R149-964	0.187	$6.12 \cdot 10^{-4}$	0.137	23
R149-965	0.131	$4.30 \cdot 10^{-4}$	0.016	26
R160-080	0.447	$1.47 \cdot 10^{-3}$	0.097	10
R160-084	0.237	$7.77 \cdot 10^{-4}$	0.022	23
R160-085	0.239	$7.82 \cdot 10^{-4}$	0.032	26
R161-101	0.782	$2.56 \cdot 10^{-3}$	0.468	10
R161-105	0.000	0	0.000	23
R161-106	0.000	0	0.000	26
R162-122	0.490	$1.61 \cdot 10^{-3}$	0.125	10
R162-126	0.234	$7.67 \cdot 10^{-4}$	0.103	23
R162-127	0.092	$3.03 \cdot 10^{-4}$	0.046	26
R163-140	0.570	$1.87 \cdot 10^{-3}$	0.231	10
R163-144	0.078	$2.57 \cdot 10^{-4}$	0.079	23
R163-145	0.026	$8.53 \cdot 10^{-5}$	0.040	26
R164-160	1.052	$3.45 \cdot 10^{-3}$	0.354	10
R164-164	0.301	$9.87 \cdot 10^{-4}$	0.062	23
R164-165	0.259	$8.51 \cdot 10^{-4}$	0.034	26

Statistics File for Wing Data, Boeing 737, 2-D model

μ = mean thickness in chord interval 50%-55% [mm]
Normalized Mean = Mean/457mm
σ = standard deviation of mean value [mm]

Run-Frame	μ [mm]	μ/length	σ [mm]	t [seconds]
R255-176	0.448	$9.79 \cdot 10^{-4}$	0.050	10
R255-180	0.105	$2.29 \cdot 10^{-4}$	0.015	23
R255-181	0.081	$1.76 \cdot 10^{-4}$	0.015	26
R256-208	0.653	$1.43 \cdot 10^{-3}$	0.143	10
R256-212	0.156	$3.41 \cdot 10^{-4}$	0.016	23
R256-213	0.155	$3.39 \cdot 10^{-4}$	0.014	26
R257-229	0.564	$1.23 \cdot 10^{-3}$	0.065	10
R257-233	0.021	$4.60 \cdot 10^{-5}$	0.018	23
R257-234	0.000	0	0.000	26
R258-263	0.611	$1.33 \cdot 10^{-3}$	0.059	10
R258-267	0.000	0	0.000	23
R258-268	0.000	0	0.000	26
R271-286	0.566	$1.23 \cdot 10^{-3}$	0.058	10
R271-290	0.031	$6.90 \cdot 10^{-5}$	0.021	23
R271-291	0.012	$2.61 \cdot 10^{-5}$	0.011	26
R272-321	0.531	$1.16 \cdot 10^{-3}$	0.143	10
R272-325	0.111	$2.43 \cdot 10^{-4}$	0.014	23
R272-326	0.081	$1.76 \cdot 10^{-4}$	0.009	26
R274-341	1.009	$2.21 \cdot 10^{-3}$	0.168	10
R274-345	0.189	$4.13 \cdot 10^{-4}$	0.008	23
R274-346	0.133	$2.90 \cdot 10^{-4}$	0.008	26
R275-377	0.763	$1.67 \cdot 10^{-3}$	0.321	10
R275-381	0.138	$3.01 \cdot 10^{-4}$	0.010	23
R275-382	0.100	$2.19 \cdot 10^{-4}$	0.017	26
R280-388	2.106	$4.61 \cdot 10^{-3}$	0.640	10
R280-400	0.229	$5.00 \cdot 10^{-4}$	0.008	23
R280-401	0.192	$4.21 \cdot 10^{-4}$	0.008	26
R281-417	1.164	$2.55 \cdot 10^{-3}$	0.152	10
R281-421	0.197	$4.31 \cdot 10^{-4}$	0.021	23
R281-422	0.141	$3.07 \cdot 10^{-4}$	0.012	26
R282-436	0.518	$1.13 \cdot 10^{-3}$	0.047	10
R282-440	0.089	$1.94 \cdot 10^{-4}$	0.012	23
R282-441	0.074	$1.61 \cdot 10^{-4}$	0.011	26

Run-Frame	μ [mm]	μ/length	σ [mm]	t [seconds]
R284-455	0.509	$1.11 \cdot 10^{-3}$	0.110	10
R284-459	0.161	$3.52 \cdot 10^{-4}$	0.023	23
R284-460	0.069	$1.51 \cdot 10^{-4}$	0.018	26
R285-474	0.395	$8.60 \cdot 10^{-4}$	0.090	10
R285-478	0.156	$3.41 \cdot 10^{-4}$	0.022	23
R285-479	0.088	$1.93 \cdot 10^{-4}$	0.018	26
R286-494	0.727	$1.59 \cdot 10^{-3}$	0.034	10
R286-498	0.268	$5.86 \cdot 10^{-4}$	0.039	23
R286-499	0.223	$4.88 \cdot 10^{-4}$	0.010	26
R287-514	0.884	$1.93 \cdot 10^{-3}$	0.377	10
R287-518	0.243	$5.31 \cdot 10^{-4}$	0.026	23
R287-519	0.199	$4.34 \cdot 10^{-4}$	0.013	26
R288-533	0.631	$1.38 \cdot 10^{-3}$	0.185	10
R288-537	0.198	$4.33 \cdot 10^{-4}$	0.018	23
R288-538	0.163	$3.57 \cdot 10^{-4}$	0.029	27
R302-555	0.819	$2.79 \cdot 10^{-3}$	0.096	10
R302-559	0.138	$3.03 \cdot 10^{-4}$	0.032	23
R302-560	0.084	$1.84 \cdot 10^{-4}$	0.021	27
R304-609	0.001	$2.41 \cdot 10^{-6}$	0.004	10
R304-613	0.064	$1.39 \cdot 10^{-4}$	0.034	23
R304-614	0.000	0	0.000	26
R305-644	0.118	$2.58 \cdot 10^{-4}$	0.042	10
R305-648	0.004	$7.70 \cdot 10^{-6}$	0.010	23
R305-649	0.034	$7.47 \cdot 10^{-5}$	0.052	26
R309-695	0.438	$9.53 \cdot 10^{-4}$	0.036	10
R309-699	0.119	$2.59 \cdot 10^{-4}$	0.018	23
R309-700	0.112	$2.45 \cdot 10^{-4}$	0.022	26
R311-723	0.698	$1.53 \cdot 10^{-3}$	0.049	10
R311-727	0.211	$4.62 \cdot 10^{-4}$	0.011	23
R311-728	0.184	$4.03 \cdot 10^{-4}$	0.010	26
R312-755	0.501	$1.09 \cdot 10^{-3}$	0.140	10
R312-759	0.196	$4.29 \cdot 10^{-4}$	0.009	23
R312-760	0.161	$3.53 \cdot 10^{-4}$	0.008	26
R313-774	1.275	$2.79 \cdot 10^{-3}$	0.876	10
R313-778	0.222	$4.85 \cdot 10^{-4}$	0.006	23
R313-779	0.205	$4.48 \cdot 10^{-4}$	0.011	26

Run-Frame	μ [mm]	μ/length	σ [mm]	t [seconds]
R314-808	2.245	$4.91 \cdot 10^{-3}$	1.006	10
R314-812	0.239	$5.22 \cdot 10^{-4}$	0.015	23
R314-813	0.219	$4.79 \cdot 10^{-4}$	0.002	26
R316-827	0.894	$1.95 \cdot 10^{-3}$	0.199	10
R316-831	0.258	$5.63 \cdot 10^{-4}$	0.032	23
R316-832	0.228	$4.98 \cdot 10^{-4}$	0.009	26
R317-860	0.787	$1.72 \cdot 10^{-3}$	0.143	10
R317-864	0.298	$6.51 \cdot 10^{-4}$	0.042	23
R317-865	0.226	$4.95 \cdot 10^{-4}$	0.008	26
R318-878	0.510	$1.11 \cdot 10^{-3}$	0.072	10
R318-882	0.277	$6.05 \cdot 10^{-4}$	0.033	23
R318-883	0.221	$4.83 \cdot 10^{-4}$	0.008	26
R319-895	0.501	$1.09 \cdot 10^{-3}$	0.070	10
R319-899	0.204	$4.47 \cdot 10^{-4}$	0.009	23
R319-900	0.197	$4.30 \cdot 10^{-4}$	0.009	26
R322-914	0.386	$8.47 \cdot 10^{-4}$	0.015	10
R322-918	0.282	$6.17 \cdot 10^{-4}$	0.042	23
R322-919	0.225	$4.91 \cdot 10^{-4}$	0.007	26
R323-951	0.306	$6.67 \cdot 10^{-4}$	0.038	10
R323-955	0.178	$3.89 \cdot 10^{-4}$	0.011	23
R323-956	0.155	$3.38 \cdot 10^{-4}$	0.012	26
R326-969	0.257	$5.61 \cdot 10^{-4}$	0.052	10
R326-973	0.113	$2.47 \cdot 10^{-4}$	0.034	23
R326-974	0.078	$1.70 \cdot 10^{-4}$	0.027	26
R327-002	0.211	$4.61 \cdot 10^{-4}$	0.010	10
R327-006	0.070	$1.53 \cdot 10^{-4}$	0.015	23
R327-007	0.076	$1.66 \cdot 10^{-4}$	0.035	26
R340-020	0.310	$6.78 \cdot 10^{-4}$	0.036	10
R340-024	0.288	$6.30 \cdot 10^{-4}$	0.026	23
R340-025	0.252	$5.51 \cdot 10^{-4}$	0.028	26
R341-040	0.429	$9.39 \cdot 10^{-4}$	0.062	10
R341-043	0.211	$4.62 \cdot 10^{-4}$	0.010	20
R341-044	0.210	$4.60 \cdot 10^{-4}$	0.015	23
R342-054	1.150	$2.52 \cdot 10^{-3}$	0.271	10
R342-058	0.290	$6.35 \cdot 10^{-4}$	0.061	20
R342-059	0.229	$5.01 \cdot 10^{-4}$	0.008	23

Run-Frame	μ [mm]	μ/length	σ [mm]	t [seconds]
R344-074	1.408	$3.08 \cdot 10^{-3}$	0.054	10
R344-078	0.215	$4.70 \cdot 10^{-4}$	0.007	23
R344-079	0.225	$4.92 \cdot 10^{-4}$	0.007	26
R345-091	2.457	$5.38 \cdot 10^{-3}$	1.235	10
R345-095	0.197	$4.31 \cdot 10^{-4}$	0.018	23
R345-096	0.210	$4.60 \cdot 10^{-4}$	0.015	26
R346-108	0.669	$1.46 \cdot 10^{-3}$	0.331	10
R346-112	0.275	$6.02 \cdot 10^{-4}$	0.034	23
R346-113	0.243	$5.32 \cdot 10^{-4}$	0.015	26
R347-126	1.182	$2.59 \cdot 10^{-3}$	0.255	10
R347-130	0.250	$5.47 \cdot 10^{-4}$	0.033	23
R347-131	0.218	$4.77 \cdot 10^{-4}$	0.007	26
R353-145	1.330	$2.84 \cdot 10^{-3}$	0.212	10
R353-149	0.507	$1.11 \cdot 10^{-3}$	0.058	23
R353-150	0.468	$1.02 \cdot 10^{-3}$	0.046	26
R354-163	0.978	$2.14 \cdot 10^{-3}$	0.251	10
R354-167	0.345	$7.55 \cdot 10^{-4}$	0.048	23
R354-168	0.277	$6.06 \cdot 10^{-4}$	0.047	26
R355-195	1.021	$2.23 \cdot 10^{-3}$	0.326	10
R355-199	0.394	$8.62 \cdot 10^{-4}$	0.025	23
R355-200	0.302	$6.61 \cdot 10^{-4}$	0.065	26
R356-227	1.146	$2.51 \cdot 10^{-3}$	0.282	10
R356-231	0.231	$5.05 \cdot 10^{-4}$	0.036	23
R356-232	0.212	$4.64 \cdot 10^{-4}$	0.066	26
R358-247	0.560	$1.23 \cdot 10^{-3}$	0.108	10
R358-251	0.212	$4.64 \cdot 10^{-4}$	0.040	23
R358-252	0.231	$5.05 \cdot 10^{-4}$	0.025	26
R359-279	0.364	$7.96 \cdot 10^{-4}$	0.070	10
R359-283	0.220	$4.81 \cdot 10^{-4}$	0.011	23
R359-284	0.159	$3.84 \cdot 10^{-4}$	0.041	26
R361-298	3.974	$8.70 \cdot 10^{-3}$	0.197	10
R361-302	0.372	$8.14 \cdot 10^{-4}$	0.054	23
R361-303	0.261	$5.71 \cdot 10^{-4}$	0.041	26
R362-331	2.212	$4.84 \cdot 10^{-3}$	1.088	10
R362-335	0.270	$5.91 \cdot 10^{-4}$	0.037	23
R362-336	0.270	$5.91 \cdot 10^{-4}$	0.037	26

Run-Frame	μ [mm]	μ/length	σ [mm]	t [seconds]
R363-348	0.651	$1.42 \cdot 10^{-3}$	0.092	10
R363-352	0.272	$5.95 \cdot 10^{-4}$	0.036	23
R363-353	0.230	$5.03 \cdot 10^{-4}$	0.010	26
R364-365	0.840	$1.84 \cdot 10^{-3}$	0.120	10
R364-369	0.327	$7.16 \cdot 10^{-4}$	0.033	23
R364-370	0.281	$6.15 \cdot 10^{-4}$	0.035	26
R365-397	0.823	$1.80 \cdot 10^{-3}$	0.122	10
R365-401	0.563	$1.23 \cdot 10^{-3}$	0.072	23
R365-402	0.405	$8.85 \cdot 10^{-4}$	0.045	26
R366-431	0.737	$1.61 \cdot 10^{-3}$	0.113	10
R366-435	0.630	$1.38 \cdot 10^{-3}$	0.097	23
R366-436	0.464	$1.02 \cdot 10^{-3}$	0.069	26
R376-454	0.668	$1.46 \cdot 10^{-3}$	0.076	10
R376-458	0.412	$9.01 \cdot 10^{-4}$	0.032	23
R376-459	0.289	$6.32 \cdot 10^{-4}$	0.032	26
R377-473	0.625	$1.37 \cdot 10^{-3}$	0.088	10
R377-477	0.292	$6.39 \cdot 10^{-4}$	0.051	23
R377-478	0.205	$4.49 \cdot 10^{-4}$	0.024	26
R381-505	0.156	$3.41 \cdot 10^{-4}$	0.003	10
R381-509	0.043	$9.51 \cdot 10^{-5}$	0.010	23
R381-510	0.051	$1.11 \cdot 10^{-4}$	0.029	26
R382-523	0.165	$3.60 \cdot 10^{-4}$	0.017	10
R382-527	0.073	$1.60 \cdot 10^{-4}$	0.021	23
R382-528	0.061	$1.34 \cdot 10^{-4}$	0.024	26
R383-543	0.064	$1.41 \cdot 10^{-4}$	0.009	10
R383-548	0.033	$7.11 \cdot 10^{-5}$	0.012	23
R383-549	0.006	$1.31 \cdot 10^{-5}$	0.008	26
R385-563	1.021	$2.24 \cdot 10^{-3}$	0.106	10
R385-567	0.289	$6.33 \cdot 10^{-4}$	0.060	23
R385-568	0.224	$4.89 \cdot 10^{-4}$	0.014	26
R386-593	0.975	$2.13 \cdot 10^{-3}$	0.132	10
R386-597	0.287	$6.29 \cdot 10^{-4}$	0.036	23
R386-598	0.210	$4.61 \cdot 10^{-4}$	0.032	26
R387-611	0.567	$1.24 \cdot 10^{-3}$	0.049	10
R387-615	0.521	$1.14 \cdot 10^{-3}$	0.043	23
R387-616	0.510	$1.12 \cdot 10^{-3}$	0.044	26

Run-Frame	μ [mm]	μ/length	σ [mm]	t [seconds]
R387-611A	0.226	$4.96 \cdot 10^{-4}$	0.008	10
R387-615A	0.236	$5.16 \cdot 10^{-4}$	0.016	23
R387-616A	0.227	$4.98 \cdot 10^{-4}$	0.008	26
R391-644	0.689	$1.51 \cdot 10^{-3}$	0.073	10
R391-648	0.599	$1.31 \cdot 10^{-3}$	0.073	23
R391-649	0.353	$7.73 \cdot 10^{-4}$	0.042	26
R392-663	0.721	$1.58 \cdot 10^{-3}$	0.176	10
R392-667	0.629	$1.38 \cdot 10^{-3}$	0.072	23
R392-668	0.493	$1.08 \cdot 10^{-3}$	0.074	26
R395-681	0.979	$2.14 \cdot 10^{-3}$	0.070	10
R395-685	0.787	$1.72 \cdot 10^{-3}$	0.105	23
R395-686	0.504	$1.10 \cdot 10^{-3}$	0.040	26
R396-699	0.640	$1.40 \cdot 10^{-3}$	0.098	10
R396-703	0.192	$4.21 \cdot 10^{-4}$	0.014	23
R396-704	0.141	$3.10 \cdot 10^{-4}$	0.012	26
R397-717	0.621	$1.36 \cdot 10^{-3}$	0.054	10
R397-721	0.277	$6.06 \cdot 10^{-4}$	0.046	23
R397-722	0.212	$4.64 \cdot 10^{-4}$	0.012	26
R398-736	0.411	$9.00 \cdot 10^{-4}$	0.022	10
R398-740	0.192	$4.20 \cdot 10^{-4}$	0.023	23
R398-741	0.113	$2.48 \cdot 10^{-4}$	0.017	26
R399-754	0.572	$1.25 \cdot 10^{-3}$	0.109	10
R399-758	0.282	$6.17 \cdot 10^{-4}$	0.066	23
R399-759	0.209	$4.57 \cdot 10^{-4}$	0.021	26
R400-772	1.256	$2.75 \cdot 10^{-3}$	0.263	10
R400-776	0.327	$7.16 \cdot 10^{-4}$	0.046	23
R400-777	0.233	$5.09 \cdot 10^{-4}$	0.023	26
R405-790	0.917	$2.01 \cdot 10^{-3}$	0.153	10
R405-794	0.223	$4.88 \cdot 10^{-4}$	0.021	23
R405-795	0.199	$4.36 \cdot 10^{-4}$	0.016	26
R406-809	0.950	$2.08 \cdot 10^{-3}$	0.275	10
R406-813	0.200	$4.37 \cdot 10^{-4}$	0.010	23
R406-814	0.181	$3.96 \cdot 10^{-4}$	0.013	26
R408-827	0.963	$2.11 \cdot 10^{-3}$	0.098	10
R408-831	0.181	$3.96 \cdot 10^{-4}$	0.009	23
R408-832	0.160	$3.49 \cdot 10^{-4}$	0.012	26

Run-Frame	μ [mm]	μ/length	σ [mm]	t [seconds]
R409-847	0.966	$2.11\cdot10^{-3}$	0.466	10
R409-851	0.139	$3.03\cdot10^{-4}$	0.012	23
R409-852	0.156	$3.41\cdot10^{-4}$	0.012	26
R410-865	0.880	$1.93\cdot10^{-3}$	0.409	10
R410-869	0.249	$5.44\cdot10^{-4}$	0.035	23
R410-870	0.206	$4.50\cdot10^{-4}$	0.024	26
R411-883	0.222	$4.87\cdot10^{-4}$	0.015	10
R411-887	0.035	$7.60\cdot10^{-5}$	0.019	23
R411-888	0.034	$7.36\cdot10^{-5}$	0.015	26
R413-899	1.010	$2.21\cdot10^{-3}$	0.220	10
R413-903	0.518	$1.13\cdot10^{-3}$	0.030	23
R413-904	0.451	$9.87\cdot10^{-4}$	0.033	26
R414-917	1.194	$2.61\cdot10^{-3}$	0.145	10
R414-921	0.215	$4.70\cdot10^{-4}$	0.007	23
R414-922	0.137	$3.00\cdot10^{-4}$	0.039	26
R429-936	0.660	$1.44\cdot10^{-3}$	0.067	10
R429-941	0.157	$3.44\cdot10^{-4}$	0.010	23
R429-942	0.124	$2.72\cdot10^{-4}$	0.010	26
R430-955	0.785	$1.72\cdot10^{-3}$	0.190	10
R430-960	0.451	$9.88\cdot10^{-4}$	0.025	23
R430-961	0.393	$8.61\cdot10^{-4}$	0.037	26
R431-974	0.659	$1.44\cdot10^{-3}$	0.121	10
R431-979	0.223	$4.87\cdot10^{-4}$	0.012	23
R431-980	0.196	$4.30\cdot10^{-4}$	0.010	26
R432-994	0.155	$3.40\cdot10^{-4}$	0.013	10
R432-999	0.126	$2.76\cdot10^{-4}$	0.036	23
R432-000	0.143	$3.14\cdot10^{-4}$	0.045	26
R434-008	0.611	$1.34\cdot10^{-3}$	0.033	10
R434-011	0.798	$1.75\cdot10^{-3}$	0.117	23
R434-012	0.469	$1.03\cdot10^{-3}$	0.028	26
R435-028	0.656	$1.44\cdot10^{-3}$	0.064	10
R435-032	0.174	$3.80\cdot10^{-4}$	0.019	23
R435-033	0.167	$3.65\cdot10^{-4}$	0.028	26
R436-045	1.340	$2.93\cdot10^{-3}$	0.103	10
R436-050	0.235	$5.15\cdot10^{-4}$	0.036	23
R436-051	0.246	$5.38\cdot10^{-4}$	0.053	26

Run-Frame	μ [mm]	μ/length	σ [mm]	t [seconds]
R438-065	0.305	$6.67 \cdot 10^{-4}$	0.029	10
R438-070	0.172	$3.76 \cdot 10^{-4}$	0.011	23
R438-071	0.136	$2.97 \cdot 10^{-4}$	0.013	26
R439-084	0.410	$8.98 \cdot 10^{-4}$	0.040	10
R439-089	0.196	$4.29 \cdot 10^{-4}$	0.011	23
R439-090	0.147	$3.22 \cdot 10^{-4}$	0.011	26
R440-103	0.647	$1.41 \cdot 10^{-3}$	0.023	10
R440-108	0.193	$4.23 \cdot 10^{-4}$	0.018	23
R440-109	0.144	$3.16 \cdot 10^{-4}$	0.017	26
R441-122	0.326	$7.14 \cdot 10^{-4}$	0.051	10
R441-127	0.056	$1.23 \cdot 10^{-4}$	0.026	23
R441-128	0.077	$1.68 \cdot 10^{-4}$	0.041	26
R446-140	0.872	$1.91 \cdot 10^{-3}$	0.262	10
R446-145	0.529	$1.16 \cdot 10^{-3}$	0.085	23
R446-146	0.392	$8.58 \cdot 10^{-4}$	0.058	26
R447-163	0.939	$2.05 \cdot 10^{-3}$	0.285	10
R447-168	0.531	$1.16 \cdot 10^{-3}$	0.085	23
R447-169	0.418	$9.16 \cdot 10^{-4}$	0.036	26
R454-008	0.843	$1.85 \cdot 10^{-3}$	0.259	10
R454-012	0.196	$4.29 \cdot 10^{-4}$	0.040	23
R454-013	0.097	$2.11 \cdot 10^{-4}$	0.024	26
R455-027	0.462	$1.01 \cdot 10^{-3}$	0.067	10
R455-031	0.120	$2.63 \cdot 10^{-4}$	0.020	23
R455-032	0.132	$2.89 \cdot 10^{-4}$	0.032	26
R457-045	1.586	$3.47 \cdot 10^{-3}$	0.742	10
R457-049	0.404	$8.85 \cdot 10^{-4}$	0.037	23
R457-050	0.315	$6.90 \cdot 10^{-4}$	0.044	26
R458-070	0.636	$1.39 \cdot 10^{-3}$	0.067	10
R458-074	0.168	$3.69 \cdot 10^{-4}$	0.021	23
R458-075	0.161	$3.51 \cdot 10^{-4}$	0.027	26
R459-087	0.786	$1.72 \cdot 10^{-3}$	0.138	10
R459-091	0.370	$8.09 \cdot 10^{-4}$	0.054	23
R459-092	0.271	$5.92 \cdot 10^{-4}$	0.043	26
R460-105	1.206	$2.64 \cdot 10^{-3}$	0.253	10
R460-109	0.389	$8.52 \cdot 10^{-4}$	0.050	23
R460-110	0.261	$5.71 \cdot 10^{-4}$	0.028	26

Statistics File for Wing Data, De Havilland DASH-8, 2-D model

μ = mean thickness in chord interval 50%-55% [mm]
Normalized Mean = $\mu/457$
σ = standard deviation of mean value [mm]

Run-Frame	μ [mm]	μ/length	σ [mm]	t [seconds]
R024-009	3.093	$6.77 \cdot 10^{-3}$	1.181	10
R024-010	0.746	$1.63 \cdot 10^{-3}$	0.475	13
R024-011	0.562	$1.23 \cdot 10^{-3}$	0.058	16
R025-025	0.003	$6.98 \cdot 10^{-6}$	0.006	10
R025-026	0.001	$2.64 \cdot 10^{-6}$	0.004	13
R025-027	0.084	$1.83 \cdot 10^{-4}$	0.039	16
R026-041	0.205	$4.48 \cdot 10^{-4}$	0.016	10
R026-042	0.208	$4.56 \cdot 10^{-4}$	0.018	13
R026-043	0.240	$5.25 \cdot 10^{-4}$	0.008	16
R028-052	0.261	$5.71 \cdot 10^{-4}$	0.035	10
R028-053	0.251	$5.49 \cdot 10^{-4}$	0.028	13
R028-054	0.256	$5.60 \cdot 10^{-4}$	0.025	16
R029-067	1.089	$2.38 \cdot 10^{-3}$	0.617	10
R029-068	0.462	$1.01 \cdot 10^{-3}$	0.064	13
R029-069	0.383	$8.37 \cdot 10^{-4}$	0.033	16
R030-082	0.233	$5.09 \cdot 10^{-4}$	0.007	10
R030-083	0.230	$5.04 \cdot 10^{-4}$	0.007	13
R030-084	0.227	$4.96 \cdot 10^{-4}$	0.008	16
R032-099	0.518	$1.13 \cdot 10^{-3}$	0.062	10
R032-100	0.440	$9.63 \cdot 10^{-4}$	0.092	13
R032-101	0.331	$7.24 \cdot 10^{-4}$	0.038	16
R033-116	0.748	$1.64 \cdot 10^{-3}$	0.099	10
R033-117	0.434	$9.50 \cdot 10^{-4}$	0.030	13
R033-118	0.269	$5.88 \cdot 10^{-4}$	0.073	16
R034-131	0.636	$1.39 \cdot 10^{-3}$	0.020	10
R034-132	0.642	$1.41 \cdot 10^{-3}$	0.025	13
R034-133	0.531	$1.16 \cdot 10^{-3}$	0.031	16
R036-150	0.739	$1.62 \cdot 10^{-3}$	0.047	10
R036-151	0.635	$1.39 \cdot 10^{-3}$	0.134	13
R036-152	0.597	$1.31 \cdot 10^{-3}$	0.104	16
R037-166	0.678	$1.48 \cdot 10^{-3}$	0.142	10
R037-167	0.572	$1.25 \cdot 10^{-3}$	0.145	13
R037-168	0.382	$8.37 \cdot 10^{-4}$	0.052	16

Run-Frame	μ [mm]	μ/length	σ [mm]	t [seconds]
R038-182	0.608	$1.33\cdot10^{-3}$	0.113	10
R038-183	0.493	$1.08\cdot10^{-3}$	0.051	13
R038-184	0.440	$9.62\cdot10^{-4}$	0.066	16
R040-199	0.563	$1.23\cdot10^{-3}$	0.078	10
R040-200	0.362	$7.91\cdot10^{-4}$	0.022	13
R040-201	0.353	$7.72\cdot10^{-4}$	0.028	16
R041-218	0.208	$4.55\cdot10^{-4}$	0.009	10
R041-219	0.169	$3.70\cdot10^{-4}$	0.008	13
R041-220	0.174	$3.80\cdot10^{-4}$	0.006	16
R061-271	0.717	$1.57\cdot10^{-3}$	0.099	10
R061-273	0.422	$9.24\cdot10^{-4}$	0.062	16
R061-274	0.361	$7.89\cdot10^{-4}$	0.049	19
R062-286	0.471	$1.03\cdot10^{-3}$	0.047	10
R062-288	0.461	$1.01\cdot10^{-3}$	0.043	16
R062-289	0.420	$9.20\cdot10^{-4}$	0.022	19
R063-303	0.733	$1.60\cdot10^{-3}$	0.116	10
R063-305	0.739	$1.62\cdot10^{-3}$	0.137	16
R063-306	0.581	$1.27\cdot10^{-3}$	0.112	19
R068-351	0.722	$1.58\cdot10^{-3}$	0.141	10
R068-353	0.533	$1.17\cdot10^{-3}$	0.064	16
R068-354	0.504	$1.10\cdot10^{-3}$	0.075	19
R076-367	0.248	$5.43\cdot10^{-4}$	0.044	10
R076-368	0.279	$6.09\cdot10^{-4}$	0.044	13
R076-369	0.236	$5.15\cdot10^{-4}$	0.040	16
R077-382	1.253	$2.65\cdot10^{-3}$	0.490	10
R077-383	2.065	$4.52\cdot10^{-3}$	0.991	13
R077-384	1.253	$2.74\cdot10^{-3}$	0.216	16
R078-398	1.110	$2.43\cdot10^{-3}$	0.419	10
R078-399	0.739	$1.62\cdot10^{-3}$	0.229	13
R078-400	0.412	$9.02\cdot10^{-4}$	0.080	16
R080-415	0.553	$1.21\cdot10^{-3}$	0.074	10
R080-416	0.345	$7.56\cdot10^{-4}$	0.021	13
R080-417	0.308	$6.74\cdot10^{-4}$	0.044	16
R081-430	0.492	$1.08\cdot10^{-3}$	0.039	10
R081-431	0.363	$7.95\cdot10^{-4}$	0.054	13
R081-432	0.297	$6.50\cdot10^{-4}$	0.029	16

Run-Frame	μ [mm]	μ/length	σ [mm]	t [seconds]
R082-445	1.575	$3.45 \cdot 10^{-3}$	0.856	10
R082-446	0.709	$1.55 \cdot 10^{-3}$	0.138	13
R082-447	0.449	$9.82 \cdot 10^{-4}$	0.070	16
R086-460	0.233	$5.09 \cdot 10^{-4}$	0.007	10
R086-461	0.242	$5.30 \cdot 10^{-4}$	0.016	13
R086-462	0.220	$4.81 \cdot 10^{-4}$	0.010	16
R087-475	0.454	$9.93 \cdot 10^{-4}$	0.057	10
R087-476	0.277	$6.06 \cdot 10^{-4}$	0.048	13
R087-477	0.209	$4.56 \cdot 10^{-4}$	0.011	16
R088-491	0.894	$1.96 \cdot 10^{-3}$	0.200	10
R088-492	0.597	$1.31 \cdot 10^{-3}$	0.118	13
R088-493	0.480	$1.05 \cdot 10^{-3}$	0.047	16
R091-507	0.975	$2.13 \cdot 10^{-3}$	0.121	10
R091-508	0.510	$1.12 \cdot 10^{-3}$	0.135	13
R091-509	0.387	$8.47 \cdot 10^{-4}$	0.055	16
R096-546	0.574	$1.26 \cdot 10^{-3}$	0.148	10
R096-547	0.321	$7.03 \cdot 10^{-4}$	0.052	13
R096-548	0.242	$5.30 \cdot 10^{-4}$	0.016	16
R097-563	0.608	$1.33 \cdot 10^{-3}$	0.072	10
R097-564	0.413	$9.04 \cdot 10^{-4}$	0.043	13
R097-565	0.279	$6.10 \cdot 10^{-4}$	0.040	16
R098-579	0.392	$8.58 \cdot 10^{-4}$	0.086	10
R098-582	0.208	$4.55 \cdot 10^{-4}$	0.007	19
R098-583	0.208	$4.54 \cdot 10^{-4}$	0.007	22
R092-523	3.043	$6.66 \cdot 10^{-3}$	1.205	10
R092-524	1.170	$2.56 \cdot 10^{-3}$	0.942	13
R092-525	0.450	$9.84 \cdot 10^{-4}$	0.056	16
R099-594	0.446	$9.76 \cdot 10^{-4}$	0.044	10
R099-596	0.229	$5.01 \cdot 10^{-4}$	0.012	16
R099-597	0.231	$5.05 \cdot 10^{-4}$	0.008	19
R101-612	1.079	$2.36 \cdot 10^{-3}$	0.215	10
R101-614	0.332	$7.27 \cdot 10^{-4}$	0.038	16
R101-615	0.323	$7.07 \cdot 10^{-4}$	0.032	19
R102-628	0.631	$1.38 \cdot 10^{-3}$	0.130	10
R102-630	0.350	$7.65 \cdot 10^{-4}$	0.046	16
R102-631	0.365	$7.99 \cdot 10^{-4}$	0.021	19

Run-Frame	μ [mm]	μ/length	σ [mm]	t [seconds]
R103-644	0.273	$5.98 \cdot 10^{-4}$	0.023	10
R103-645	0.282	$6.17 \cdot 10^{-4}$	0.043	13
R103-646	0.213	$4.67 \cdot 10^{-4}$	0.016	16
R110-664	0.551	$1.21 \cdot 10^{-3}$	0.123	10
R110-665	0.398	$8.71 \cdot 10^{-4}$	0.084	13
R110-666	0.319	$6.97 \cdot 10^{-4}$	0.064	16
R111-679	0.338	$7.40 \cdot 10^{-4}$	0.040	10
R111-680	0.232	$5.07 \cdot 10^{-4}$	0.022	13
R111-681	0.242	$5.30 \cdot 10^{-4}$	0.025	16
R112-693	0.712	$1.56 \cdot 10^{-3}$	0.240	10
R112-694	0.504	$1.10 \cdot 10^{-3}$	0.076	13
R112-695	0.478	$1.05 \cdot 10^{-3}$	0.072	16
R115-714	0.517	$1.13 \cdot 10^{-3}$	0.149	10
R115-715	0.388	$8.50 \cdot 10^{-4}$	0.107	13
R115-716	0.332	$7.27 \cdot 10^{-4}$	0.070	16
R116-730	0.268	$5.87 \cdot 10^{-4}$	0.045	10
R116-731	0.236	$5.17 \cdot 10^{-4}$	0.015	13
R116-732	0.251	$5.49 \cdot 10^{-4}$	0.047	16
R117-744	0.190	$4.17 \cdot 10^{-4}$	0.025	10
R117-745	0.152	$3.32 \cdot 10^{-4}$	0.038	13
R117-746	0.262	$5.74 \cdot 10^{-4}$	0.041	16
R118-759	0.254	$5.55 \cdot 10^{-4}$	0.066	10
R118-760	0.214	$4.68 \cdot 10^{-4}$	0.028	13
R118-761	0.181	$3.96 \cdot 10^{-4}$	0.030	16
R122-775	0.460	$1.01 \cdot 10^{-3}$	0.048	10
R122-777	0.252	$5.50 \cdot 10^{-4}$	0.030	16
R122-778	0.190	$4.16 \cdot 10^{-4}$	0.021	19
R123-792	0.852	$1.87 \cdot 10^{-3}$	0.344	10
R123-794	0.615	$1.35 \cdot 10^{-3}$	0.065	16
R123-795	0.483	$1.06 \cdot 10^{-3}$	0.094	19
R124-808	0.237	$5.18 \cdot 10^{-4}$	0.032	10
R124-810	0.203	$4.44 \cdot 10^{-4}$	0.021	16
R124-811	0.163	$3.57 \cdot 10^{-4}$	0.034	19
R127-823	0.584	$1.28 \cdot 10^{-3}$	0.168	10
R127-825	0.179	$3.93 \cdot 10^{-4}$	0.017	16
R127-826	0.169	$3.70 \cdot 10^{-4}$	0.016	19

Run-Frame	μ [mm]	μ/length	σ [mm]	t [seconds]
R128-839	0.497	$1.09 \cdot 10^{-3}$	0.013	10
R128-847	0.170	$3.72 \cdot 10^{-4}$	0.017	34
R128-848	0.173	$3.79 \cdot 10^{-4}$	0.011	37
R129-858	0.269	$5.88 \cdot 10^{-4}$	0.045	10
R129-860	0.213	$4.67 \cdot 10^{-4}$	0.009	16
R129-861	0.199	$4.36 \cdot 10^{-4}$	0.007	19
R132-875	0.521	$1.14 \cdot 10^{-3}$	0.075	10
R132-877	0.348	$7.61 \cdot 10^{-4}$	0.062	16
R132-878	0.353	$7.73 \cdot 10^{-4}$	0.066	19
R133-890	0.243	$5.33 \cdot 10^{-4}$	0.032	10
R133-892	0.192	$4.21 \cdot 10^{-4}$	0.008	16
R133-893	0.194	$4.24 \cdot 10^{-4}$	0.014	19
R134-906	0.531	$1.16 \cdot 10^{-3}$	0.120	10
R134-908	0.225	$4.93 \cdot 10^{-4}$	0.033	16
R134-909	0.162	$3.55 \cdot 10^{-4}$	0.016	19
R136-921	0.196	$4.29 \cdot 10^{-4}$	0.014	10
R136-923	0.136	$2.98 \cdot 10^{-4}$	0.023	16
R136-924	0.147	$3.23 \cdot 10^{-4}$	0.030	19
R137-935	0.217	$4.74 \cdot 10^{-4}$	0.016	10
R137-937	0.130	$2.85 \cdot 10^{-4}$	0.025	16
R137-938	0.119	$2.60 \cdot 10^{-4}$	0.024	19
R140-965	0.457	$9.99 \cdot 10^{-4}$	0.033	10
R140-966	0.257	$5.63 \cdot 10^{-4}$	0.028	13
R140-967	0.228	$5.00 \cdot 10^{-4}$	0.008	16
R141-980	0.066	$1.44 \cdot 10^{-4}$	0.026	10
R141-982	0.201	$4.40 \cdot 10^{-4}$	0.019	16
R141-983	0.183	$4.00 \cdot 10^{-4}$	0.030	19
R142-996	0.471	$1.03 \cdot 10^{-3}$	0.078	10
R142-998	0.208	$4.55 \cdot 10^{-4}$	0.013	16
R142-999	0.213	$4.66 \cdot 10^{-4}$	0.014	19
R150-020	1.491	$3.26 \cdot 10^{-3}$	1.057	10
R150-022	0.996	$2.18 \cdot 10^{-3}$	0.428	16
R150-023	0.513	$1.12 \cdot 10^{-3}$	0.117	19
R151-037	2.836	$6.20 \cdot 10^{-3}$	1.248	10
R151-039	0.427	$9.34 \cdot 10^{-4}$	0.056	16
R151-040	0.390	$8.53 \cdot 10^{-4}$	0.042	19

Run-Frame	μ [mm]	μ/length	σ [mm]	t [seconds]
R152-052	0.510	$1.12 \cdot 10^{-3}$	0.108	10
R152-054	0.223	$4.87 \cdot 10^{-4}$	0.016	16
R152-055	0.210	$4.59 \cdot 10^{-4}$	0.008	19
R155-072	0.493	$1.08 \cdot 10^{-3}$	0.064	10
R155-074	0.315	$6.89 \cdot 10^{-4}$	0.051	16
R155-075	0.326	$7.14 \cdot 10^{-4}$	0.056	19
R156-087	0.483	$1.06 \cdot 10^{-3}$	0.039	10
R156-089	0.491	$1.07 \cdot 10^{-3}$	0.068	16
R156-090	0.504	$1.10 \cdot 10^{-3}$	0.099	19
R157-102	0.678	$1.48 \cdot 10^{-3}$	0.118	10
R157-106	0.342	$7.48 \cdot 10^{-4}$	0.045	23
R157-107	0.342	$7.49 \cdot 10^{-4}$	0.069	26
R158-118	0.366	$8.00 \cdot 10^{-4}$	0.045	10
R158-120	0.220	$4.82 \cdot 10^{-4}$	0.019	16
R158-121	0.226	$4.93 \cdot 10^{-4}$	0.024	19
R160-138	0.463	$1.01 \cdot 10^{-3}$	0.051	10
R160-140	0.408	$8.92 \cdot 10^{-4}$	0.042	16
R160-141	0.321	$7.01 \cdot 10^{-4}$	0.032	19
R161-154	0.240	$5.25 \cdot 10^{-4}$	0.012	10
R161-156	0.228	$4.99 \cdot 10^{-4}$	0.008	16
R161-157	0.216	$4.72 \cdot 10^{-4}$	0.007	19
R162-170	0.504	$1.10 \cdot 10^{-3}$	0.056	10
R162-171	0.549	$1.20 \cdot 10^{-3}$	0.069	13
R162-172	0.325	$7.12 \cdot 10^{-4}$	0.050	16
R164-184	0.449	$9.82 \cdot 10^{-4}$	0.042	10
R164-186	0.197	$4.30 \cdot 10^{-4}$	0.016	16
R164-187	0.115	$2.53 \cdot 10^{-4}$	0.017	19
R165-199	0.331	$7.24 \cdot 10^{-4}$	0.049	10
R165-201	0.186	$4.06 \cdot 10^{-4}$	0.021	16
R165-202	0.107	$2.34 \cdot 10^{-4}$	0.021	19
R168-214	1.628	$3.56 \cdot 10^{-3}$	0.669	10
R168-215	2.045	$4.48 \cdot 10^{-3}$	1.381	13
R168-216	1.683	$3.68 \cdot 10^{-3}$	1.008	16
R169-230	0.675	$1.48 \cdot 10^{-3}$	0.030	10
R169-231	1.399	$3.06 \cdot 10^{-3}$	0.838	13
R169-232	0.878	$1.92 \cdot 10^{-3}$	0.176	16

Run-Frame	μ [mm]	μ/length	σ [mm]	t [seconds]
R170-244	0.890	$1.95 \cdot 10^{-3}$	0.233	10
R170-245	0.447	$9.77 \cdot 10^{-4}$	0.051	13
R170-246	0.420	$9.19 \cdot 10^{-4}$	0.026	16
R172-260	0.485	$1.06 \cdot 10^{-3}$	0.017	10
R172-261	0.822	$1.80 \cdot 10^{-3}$	0.111	13
R172-262	0.860	$1.88 \cdot 10^{-3}$	0.136	16
R174-298	0.431	$9.42 \cdot 10^{-4}$	0.041	10
R174-299	0.470	$1.03 \cdot 10^{-3}$	0.074	13
R174-300	0.421	$9.22 \cdot 10^{-4}$	0.040	16
R175-313	1.001	$2.19 \cdot 10^{-3}$	0.140	10
R175-314	0.674	$1.47 \cdot 10^{-3}$	0.040	13
R175-315	0.505	$1.11 \cdot 10^{-3}$	0.104	16
R177-329	0.416	$9.11 \cdot 10^{-4}$	0.042	10
R177-330	0.482	$1.05 \cdot 10^{-3}$	0.070	13
R177-331	0.415	$9.07 \cdot 10^{-4}$	0.052	16
R178-345	0.269	$5.88 \cdot 10^{-4}$	0.039	10
R178-346	0.273	$5.97 \cdot 10^{-4}$	0.039	13
R178-347	0.302	$6.61 \cdot 10^{-4}$	0.054	16
R179-364	0.450	$9.85 \cdot 10^{-4}$	0.077	10
R179-365	0.289	$6.31 \cdot 10^{-4}$	0.055	13
R179-366	0.188	$4.11 \cdot 10^{-4}$	0.019	16
R180-379	0.215	$4.70 \cdot 10^{-4}$	0.016	10
R180-380	0.151	$3.29 \cdot 10^{-4}$	0.020	13
R180-381	0.110	$2.40 \cdot 10^{-4}$	0.027	16
R186-404	0.746	$1.63 \cdot 10^{-3}$	0.164	10
R186-406	1.146	$2.51 \cdot 10^{-3}$	0.157	16
R186-407	1.114	$2.44 \cdot 10^{-3}$	0.103	19
R187-420	0.271	$5.93 \cdot 10^{-4}$	0.088	10
R187-422	0.362	$7.92 \cdot 10^{-4}$	0.043	16
R187-423	0.319	$6.98 \cdot 10^{-4}$	0.051	19
R188-435	0.854	$1.87 \cdot 10^{-3}$	0.186	10
R188-437	0.739	$1.62 \cdot 10^{-3}$	0.137	16
R188-438	0.711	$1.56 \cdot 10^{-3}$	0.100	19
R191-452	0.228	$5.00 \cdot 10^{-4}$	0.026	10
R191-454	0.224	$4.91 \cdot 10^{-4}$	0.055	16
R191-455	0.195	$4.26 \cdot 10^{-4}$	0.027	19

Run-Frame	μ [mm]	μ/length	σ [mm]	t [seconds]
R192-467	0.070	$1.53 \cdot 10^{-4}$	0.011	10
R192-469	0.059	$1.29 \cdot 10^{-4}$	0.010	16
R192-470	0.006	$1.39 \cdot 10^{-5}$	0.008	19
R193-482	0.303	$6.64 \cdot 10^{-4}$	0.040	10
R193-483	0.370	$8.10 \cdot 10^{-4}$	0.042	13
R193-484	0.306	$6.69 \cdot 10^{-4}$	0.029	16
R196-498	0.428	$9.36 \cdot 10^{-4}$	0.037	10
R196-499	0.644	$1.41 \cdot 10^{-3}$	0.096	13
R196-500	0.547	$1.20 \cdot 10^{-3}$	0.092	16
R200-513	0.517	$1.13 \cdot 10^{-3}$	0.039	10
R200-514	0.546	$1.20 \cdot 10^{-3}$	0.059	13
R200-515	0.612	$1.34 \cdot 10^{-3}$	0.053	16
R201-528	0.475	$1.04 \cdot 10^{-3}$	0.092	10
R201-529	0.458	$1.00 \cdot 10^{-3}$	0.074	13
R201-530	0.514	$1.13 \cdot 10^{-3}$	0.120	16
R202-543	1.165	$2.55 \cdot 10^{-3}$	0.337	10
R202-544	1.050	$2.30 \cdot 10^{-3}$	0.221	13
R202-545	0.675	$1.48 \cdot 10^{-3}$	0.073	16
R205-558	0.205	$4.49 \cdot 10^{-4}$	0.014	10
R205-559	0.232	$5.08 \cdot 10^{-4}$	0.032	13
R205-560	0.191	$4.18 \cdot 10^{-4}$	0.037	16
R206-573	0.012	$2.66 \cdot 10^{-5}$	0.007	10
R206-574	0.006	$1.23 \cdot 10^{-5}$	0.008	13
R206-575	0.074	$1.63 \cdot 10^{-4}$	0.043	16
R207-588	0.330	$7.21 \cdot 10^{-4}$	0.026	10
R207-589	0.324	$7.10 \cdot 10^{-4}$	0.035	13
R207-590	0.323	$7.07 \cdot 10^{-4}$	0.049	16
R210-603	0.474	$1.04 \cdot 10^{-3}$	0.034	10
R210-604	0.565	$1.24 \cdot 10^{-3}$	0.067	13
R210-605	0.786	$1.72 \cdot 10^{-3}$	0.107	16
R220-627	0.511	$1.12 \cdot 10^{-3}$	0.054	10
R220-628	0.518	$1.13 \cdot 10^{-3}$	0.067	13
R220-629	0.414	$9.06 \cdot 10^{-4}$	0.044	16
R221-652	1.067	$2.34 \cdot 10^{-3}$	0.199	10
R221-653	0.703	$1.54 \cdot 10^{-3}$	0.137	13
R221-654	0.469	$1.03 \cdot 10^{-3}$	0.070	16

Run-Frame	μ [mm]	μ/length	σ [mm]	t [seconds]
R222-667	0.653	$1.43\cdot10^{-3}$	0.033	10
R222-668	1.084	$2.37\cdot10^{-3}$	0.283	13
R222-669	0.734	$1.61\cdot10^{-3}$	0.185	16
R225-682	0.791	$1.73\cdot10^{-3}$	0.133	10
R225-683	0.686	$1.50\cdot10^{-3}$	0.089	13
R225-684	0.490	$1.07\cdot10^{-3}$	0.080	16
R226-702	2.764	$6.05\cdot10^{-3}$	1.149	10
R226-703	3.528	$7.72\cdot10^{-3}$	0.996	13
R226-704	1.444	$3.16\cdot10^{-3}$	1.039	16
R227-722	1.209	$2.65\cdot10^{-3}$	0.307	10
R227-723	1.258	$2.75\cdot10^{-3}$	0.155	13
R227-724	1.555	$3.40\cdot10^{-3}$	0.118	16
R226-702	2.764	$6.05\cdot10^{-3}$	1.149	10
R226-703	3.528	$7.72\cdot10^{-3}$	0.996	13
R226-704	1.444	$3.16\cdot10^{-3}$	1.039	16
R230-737	0.755	$1.65\cdot10^{-3}$	0.125	10
R230-739	1.025	$2.24\cdot10^{-3}$	0.174	16
R230-740	0.904	$1.98\cdot10^{-3}$	0.129	19
R231-752	0.480	$1.05\cdot10^{-3}$	0.061	10
R231-754	0.495	$1.08\cdot10^{-3}$	0.069	16
R231-755	0.347	$7.60\cdot10^{-4}$	0.051	19
R234-767	0.549	$1.20\cdot10^{-3}$	0.074	10
R234-768	0.674	$1.48\cdot10^{-3}$	0.048	13
R234-769	0.602	$1.32\cdot10^{-3}$	0.059	16
R235-782	0.643	$1.41\cdot10^{-3}$	0.104	10
R235-783	0.708	$1.55\cdot10^{-3}$	0.127	13
R235-784	0.526	$1.15\cdot10^{-3}$	0.092	16
R236-797	0.305	$6.68\cdot10^{-4}$	0.052	10
R236-798	0.414	$9.05\cdot10^{-4}$	0.020	13
R236-799	0.447	$9.79\cdot10^{-4}$	0.019	16
R239-814	2.356	$5.15\cdot10^{-3}$	1.250	10
R239-815	3.852	$8.43\cdot10^{-3}$	0.553	13
R239-816	3.556	$7.78\cdot10^{-3}$	0.844	16
R240-830	0.477	$1.04\cdot10^{-3}$	0.045	10
R240-831	0.612	$1.34\cdot10^{-3}$	0.075	13
R240-832	0.505	$1.11\cdot10^{-3}$	0.093	16

Run-Frame	μ [mm]	μ/length	σ [mm]	t [seconds]
R241-853	0.518	$1.13 \cdot 10^{-3}$	0.090	10
R241-854	0.510	$1.12 \cdot 10^{-3}$	0.058	13
R241-855	0.660	$1.44 \cdot 10^{-3}$	0.095	16
R241-868	0.691	$1.51 \cdot 10^{-3}$	0.031	10
R241-869	0.943	$2.06 \cdot 10^{-3}$	0.311	13
R241-870	1.322	$2.89 \cdot 10^{-3}$	0.341	16
R245-883	2.813	$6.15 \cdot 10^{-3}$	1.366	10
R245-884	1.480	$3.24 \cdot 10^{-3}$	0.775	13
R245-885	0.872	$1.91 \cdot 10^{-3}$	0.239	16
R246-902	0.715	$1.56 \cdot 10^{-3}$	0.314	10
R246-903	0.887	$1.94 \cdot 10^{-3}$	0.098	13
R246-904	0.778	$1.70 \cdot 10^{-3}$	0.134	16
R249-937	0.521	$1.14 \cdot 10^{-3}$	0.135	10
R249-938	0.557	$1.22 \cdot 10^{-3}$	0.084	13
R249-939	0.547	$1.20 \cdot 10^{-3}$	0.081	16
R250-952	0.568	$1.24 \cdot 10^{-3}$	0.055	10
R250-953	0.583	$1.28 \cdot 10^{-3}$	0.076	13
R250-954	0.624	$1.36 \cdot 10^{-3}$	0.066	16
R251-968	0.573	$1.25 \cdot 10^{-3}$	0.091	10
R251-969	0.702	$1.54 \cdot 10^{-3}$	0.103	13
R251-970	0.595	$1.30 \cdot 10^{-3}$	0.054	16
R283-008	0.452	$9.89 \cdot 10^{-4}$	0.025	10
R283-009	0.510	$1.12 \cdot 10^{-3}$	0.084	13
R283-010	0.460	$1.01 \cdot 10^{-3}$	0.031	16
R284-033	1.438	$3.15 \cdot 10^{-3}$	0.213	10
R284-034	1.466	$3.21 \cdot 10^{-3}$	0.779	13
R284-035	0.858	$1.88 \cdot 10^{-3}$	0.211	16
R287-051	0.459	$1.00 \cdot 10^{-3}$	0.023	10
R287-052	0.524	$1.15 \cdot 10^{-3}$	0.081	13
R287-053	0.415	$9.09 \cdot 10^{-4}$	0.038	16
R297-065	0.479	$1.05 \cdot 10^{-3}$	0.024	10
R297-066	0.630	$1.38 \cdot 10^{-3}$	0.088	13
R297-067	0.620	$1.36 \cdot 10^{-3}$	0.076	16
R298-080	1.437	$3.14 \cdot 10^{-3}$	0.636	10
R298-081	2.615	$5.72 \cdot 10^{-3}$	0.936	13
R298-082	2.320	$5.08 \cdot 10^{-3}$	1.007	16

Run-Frame	μ [mm]	μ/length	σ [mm]	t [seconds]
R299-093	0.523	$1.14\cdot10^{-3}$	0.023	4
R299-094	0.511	$1.12\cdot10^{-3}$	0.019	7
R299-095	0.512	$1.12\cdot10^{-3}$	0.062	10
R305-128	1.129	$2.47\cdot10^{-3}$	0.664	10
R305-129	3.347	$7.32\cdot10^{-3}$	0.988	13
R305-130	2.725	$5.96\cdot10^{-3}$	1.029	16
R310-143	0.544	$1.19\cdot10^{-3}$	0.076	10
R310-144	0.498	$1.09\cdot10^{-3}$	0.067	13
R310-145	0.490	$1.07\cdot10^{-3}$	0.077	16
R311-159	3.305	$7.23\cdot10^{-3}$	0.673	10
R311-161	0.897	$1.96\cdot10^{-3}$	0.302	16
R311-162	0.682	$1.49\cdot10^{-3}$	0.136	19
R312-177	0.906	$1.98\cdot10^{-3}$	0.313	10
R312-178	0.666	$1.46\cdot10^{-3}$	0.167	13
R312-179	0.646	$1.41\cdot10^{-3}$	0.053	16
R317-192	0.583	$1.28\cdot10^{-3}$	0.067	10
R317-193	0.769	$1.68\cdot10^{-3}$	0.158	13
R317-194	0.815	$1.78\cdot10^{-3}$	0.142	16
R318-207	1.100	$2.41\cdot10^{-3}$	0.347	10
R318-208	1.591	$3.48\cdot10^{-3}$	0.998	13
R318-209	2.479	$5.42\cdot10^{-3}$	1.175	16
R321-224	0.509	$1.11\cdot10^{-3}$	0.085	10
R321-225	0.713	$1.56\cdot10^{-3}$	0.160	13
R321-226	0.587	$1.28\cdot10^{-3}$	0.079	16
R322-239	0.698	$1.53\cdot10^{-3}$	0.126	10
R322-240	1.258	$2.75\cdot10^{-3}$	0.652	13
R322-241	1.686	$3.69\cdot10^{-3}$	0.983	16
R323-255	0.906	$1.98\cdot10^{-3}$	0.282	10
R323-256	1.029	$2.25\cdot10^{-3}$	0.132	13
R323-257	1.033	$2.26\cdot10^{-3}$	0.149	16
R329-272	0.641	$1.40\cdot10^{-3}$	0.024	10
R329-273	1.126	$2.46\cdot10^{-3}$	0.452	13
R329-274	1.554	$3.40\cdot10^{-3}$	0.381	16
R330-285	0.708	$1.55\cdot10^{-3}$	0.042	10
R330-286	0.756	$1.65\cdot10^{-3}$	0.092	13
R330-287	0.833	$1.82\cdot10^{-3}$	0.071	16

Run-Frame	μ [mm]	μ/length	σ [mm]	t [seconds]
R333-304	0.456	$9.99 \cdot 10^{-4}$	0.022	10
R333-305	0.573	$1.25 \cdot 10^{-3}$	0.107	13
R333-306	0.727	$1.59 \cdot 10^{-3}$	0.157	16
R335-339	0.524	$1.15 \cdot 10^{-3}$	0.073	10
R335-340	0.572	$1.25 \cdot 10^{-3}$	0.104	13
R335-341	1.232	$2.70 \cdot 10^{-3}$	0.362	16
R340-355	0.387	$8.47 \cdot 10^{-4}$	0.047	10
R340-356	0.354	$7.75 \cdot 10^{-4}$	0.064	13
R340-357	0.422	$9.24 \cdot 10^{-4}$	0.094	16
R341-374	0.193	$4.22 \cdot 10^{-4}$	0.009	10
R341-375	0.194	$4.24 \cdot 10^{-4}$	0.014	13
R341-376	0.206	$4.51 \cdot 10^{-4}$	0.012	16
R342-390	0.682	$1.49 \cdot 10^{-3}$	0.042	10
R342-391	0.615	$1.35 \cdot 10^{-3}$	0.105	13
R342-392	0.655	$1.43 \cdot 10^{-3}$	0.134	16
R347-432	0.452	$9.89 \cdot 10^{-4}$	0.024	10
R347-433	0.451	$9.87 \cdot 10^{-4}$	0.032	13
R347-434	0.475	$1.04 \cdot 10^{-3}$	0.052	16
R348-447	0.173	$3.79 \cdot 10^{-4}$	0.014	10
R348-448	0.168	$3.68 \cdot 10^{-4}$	0.017	13
R348-449	0.176	$3.85 \cdot 10^{-4}$	0.015	16
R349-462	0.689	$1.51 \cdot 10^{-3}$	0.049	10
R349-463	0.739	$1.62 \cdot 10^{-3}$	0.177	13
R349-464	0.721	$1.58 \cdot 10^{-3}$	0.098	16
R350-479	0.321	$7.02 \cdot 10^{-4}$	0.017	10
R350-480	0.319	$6.98 \cdot 10^{-4}$	0.043	13
R350-481	0.382	$8.36 \cdot 10^{-4}$	0.080	16
R360-492	0.770	$1.69 \cdot 10^{-3}$	0.093	3
R360-493	0.805	$1.76 \cdot 10^{-3}$	0.092	6
R360-494	0.775	$1.70 \cdot 10^{-3}$	0.174	10
R362-517	0.746	$1.63 \cdot 10^{-3}$	0.090	10
R362-518	0.713	$1.56 \cdot 10^{-3}$	0.065	13
R362-519	0.685	$1.50 \cdot 10^{-3}$	0.090	16
R366-534	0.283	$6.18 \cdot 10^{-4}$	0.076	10
R366-535	0.313	$6.86 \cdot 10^{-4}$	0.022	13
R366-536	0.446	$9.76 \cdot 10^{-4}$	0.060	16

Run-Frame	μ [mm]	μ/length	σ [mm]	t [seconds]
R367-549	0.507	$1.11\cdot10^{-3}$	0.056	10
R367-550	0.500	$1.09\cdot10^{-3}$	0.082	13
R367-551	0.481	$1.05\cdot10^{-3}$	0.067	16
R377-565	0.466	$1.02\cdot10^{-3}$	0.076	10
R377-567	0.379	$8.29\cdot10^{-4}$	0.053	16
R377-570	0.414	$9.07\cdot10^{-4}$	0.048	26
R379-592	0.670	$1.47\cdot10^{-3}$	0.036	10
R379-593	0.662	$1.45\cdot10^{-3}$	0.035	13
R379-594	0.686	$1.50\cdot10^{-3}$	0.056	16
R383-613	0.549	$1.20\cdot10^{-3}$	0.088	10
R383-614	0.512	$1.12\cdot10^{-3}$	0.094	13
R383-615	0.498	$1.09\cdot10^{-3}$	0.057	16
R384-628	0.592	$1.29\cdot10^{-3}$	0.090	10
R384-629	0.538	$1.18\cdot10^{-3}$	0.073	13
R384-630	0.458	$1.00\cdot10^{-3}$	0.036	16
R388-644	0.558	$1.22\cdot10^{-3}$	0.069	10
R388-645	0.660	$1.44\cdot10^{-3}$	0.056	13
R388-646	0.662	$1.45\cdot10^{-3}$	0.092	16
R389-659	0.538	$1.18\cdot10^{-3}$	0.076	10
R389-660	0.754	$1.65\cdot10^{-3}$	0.139	13
R389-661	0.690	$1.51\cdot10^{-3}$	0.034	16
R392-677	0.573	$1.25\cdot10^{-3}$	0.084	10
R392-678	0.641	$1.40\cdot10^{-3}$	0.087	13
R392-679	0.735	$1.61\cdot10^{-3}$	0.103	16
R393-692	0.688	$1.50\cdot10^{-3}$	0.070	10
R393-693	0.908	$1.99\cdot10^{-3}$	0.136	13
R393-694	0.960	$2.10\cdot10^{-3}$	0.113	16
R397-707	0.606	$1.33\cdot10^{-3}$	0.107	10
R397-708	0.738	$1.61\cdot10^{-3}$	0.085	13
R397-709	0.961	$2.10\cdot10^{-3}$	0.168	16
R398-722	0.643	$1.41\cdot10^{-3}$	0.060	10
R398-723	0.860	$1.88\cdot10^{-3}$	0.324	13
R398-724	1.001	$2.19\cdot10^{-3}$	0.311	16
R402-738	0.482	$1.05\cdot10^{-3}$	0.035	10
R402-739	0.683	$1.50\cdot10^{-3}$	0.143	13
R402-740	0.640	$1.40\cdot10^{-3}$	0.105	16

Run-Frame	μ [mm]	μ/length	σ [mm]	t [seconds]
R403-753	0.934	$2.04 \cdot 10^{-3}$	0.309	10
R403-754	0.774	$1.69 \cdot 10^{-3}$	0.103	13
R403-755	0.790	$1.73 \cdot 10^{-3}$	0.085	16
R407-767	0.535	$1.17 \cdot 10^{-3}$	0.068	10
R407-768	0.508	$1.11 \cdot 10^{-3}$	0.062	13
R407-769	0.610	$1.34 \cdot 10^{-3}$	0.163	16
R408-782	0.664	$1.45 \cdot 10^{-3}$	0.021	10
R408-783	0.674	$1.48 \cdot 10^{-3}$	0.102	13
R408-784	0.824	$1.80 \cdot 10^{-3}$	0.232	16
R411-797	0.494	$1.08 \cdot 10^{-3}$	0.034	10
R411-798	0.498	$1.09 \cdot 10^{-3}$	0.065	13
R411-799	0.525	$1.15 \cdot 10^{-3}$	0.059	16
R412-812	0.475	$1.04 \cdot 10^{-3}$	0.048	10
R412-813	0.448	$9.80 \cdot 10^{-4}$	0.034	13
R412-814	0.464	$1.02 \cdot 10^{-3}$	0.035	16
R413-828	0.515	$1.13 \cdot 10^{-3}$	0.043	10
R413-829	0.516	$1.13 \cdot 10^{-3}$	0.110	13
R413-830	0.546	$1.19 \cdot 10^{-3}$	0.072	16

NASA
National Aeronautics and Space Administration

Report Documentation Page

1. Report No. NASA CR-189234	2. Government Accession No.	3. Recipient's Catalog No.
4. Title and Subtitle Digital Analysis of Wind Tunnel Imagery to Measure Fluid Thickness		5. Report Date
		6. Performing Organization Code
7. Author(s) Roger L. Easton, Jr. and James Enge		8. Performing Organization Report No. None
		10. Work Unit No.
9. Performing Organization Name and Address Center for Imaging Science, Rochester Institute of Technology, Rochester, NY 14623-0889		11. Contract or Grant No. NAG3-1202
12. Sponsoring Agency Name and Address National Aeronautics and Space Administration, Lewis Research Center, Cleveland, Ohio 44135-3191		13. Type of Report and Period Covered Contractor Report Final
		14. Sponsoring Agency Code

15. Supplementary Notes

Project Manager, Jaiwon Shin
Icing and Cryogenic Technology Branch
Lewis Research Center

16. Abstract

This report documents the procedure and results obtained from the application of digital image processing techniques to the problem of measuring the thickness of a deicing fluid on a model airfoil during simulated takeoffs. The fluid contained a fluorescent dye and the images were recorded under flash illumination on photographic film. The films were digitized and analyzed on a personal computer to obtain maps of the fluid thickness.

17. Key Words (Suggested by Author(s))	18. Distribution Statement
digital image processing deicing fluid thickness	Unclassified - Unlimited Subject Category 02

19. Security Classif. (of this report)	20. Security Classif. (of this page)	21. No of pages	22. Price*
Unclassified	Unclassified	41	A03

NASA FORM 1626 OCT 86

*For sale by the National Technical Information Service, Springfield, Virginia 22161

B-0002
December 1987